Total MMP-9 amounted to 38.2 ± 10.6 ng/mg of protein in the control group and 35.6 ± 8.22 ng/mg of protein in the Kurozu group. However, it was significantly reduced to 21.5 ± 6.1 ng/mg of protein by administration of Kurozu-M ($P < 0.05$ versus control; Fig. 3B). Activated MMP-9 amounted to 1.6 ± 0.5 ng/mg of protein in the control group, 1.4 ± 0.6 ng/mg of protein in the Kurozu group, and 0.7 ± 0.2 ng/mg of protein in the Kurozu-M group ($P < 0.05$ for the Kurozu-M group versus control; Fig. 3B).

Discussion

Our results indicate that the administration of Kurozu-M inhibits the development of colon cancer in human colon cancer cell transplantation model in mice. Further, the administration of Kurozu-M inhibited nitrotyrosine production, decreased total MMP-2 and total MMP-9 levels, and inhibited activation of MMP-2 and MMP-9 in the lesion in this model.

Earlier studies had indicated that extract of Kurozu can inhibit chemical carcinogenesis [3,4,6]. However, in our study, the administration of Kurozu-M inhibited the development of colon cancer in a mouse model, whereas the administration of Kurozu did not prevent tumor growth. The major constituent of Kurozu is acetic acid, whereas the major component of Kurozu-M is a complex mixture of organic materials, including bacterial metabolites. The active components of Kurozu-M remain to be identified.

In this study, we found that administration of Kurozu-M inhibited production of nitrotyrosine in tumor tissue. Nitrotyrosine is generated through two pathways in vivo. One is the peroxynitrite pathway, in which tyrosine reacts with peroxynitrite to afford nitrotyrosine, and the second is the myeloperoxidase pathway, in which tyrosine reacts with myeloperoxidase and nitrite [7,8]. We previously reported that peroxynitrite is produced in human colon cancer tissue [5]. In contrast, myeloperoxidase is localized in polymorphonuclear leukocytes in vivo, but in this study we could not detect any accumulation of polymorphonuclear leukocytes by means of HE staining of cancerous tissue. Therefore, Kurozu-M administration may inhibit the peroxynitrite pathway. Possible mechanisms include inhibition of nitric oxide, superoxide, and/or peroxynitrite production, and scavenging of nitric oxide, superoxide, and/or peroxynitrite. Further work is needed to examine these possibilities.

The administration of Kurozu-M also inhibited MMP-2 and MMP-9 activity in cancerous tissue. These are representative gelatinases that contribute to the distant metastasis of cancer [9], and they are produced by cancer cells or macrophages [10]. A tetradecanoylphorbol acetate-responsive element is present in the promoter region of MMP-9 and is activated by various cytokines, such as interleukin and tumor necrosis factor [11]. In addition, MMP-9 is activated by nuclear factor-κB and MMP-2 [12]. MMP-2 is mainly activated by MT1-MMP, but recently it was shown that peroxynitrite also activates MMP-2 [13,14]. Kurozu-M may have inhibited cancer growth in our model through inhibition of peroxynitrite formation and MMP-2 and MMP-9 activities.

Kurozu moromimatsu was active against Lovo cells in this study, but not against DLD-1 cells. Lovo and DLD-1 cells differ not only in the degree of cellular differentiation but also in the expression of furin, which contributes to MMP activation [15]. The former line originates from well-differentiated adenocarcinoma and expresses furin protein, whereas the latter originates from poorly differentiated adenocarcinoma and does not express furin protein. It would be worth examining whether MMP activity is reduced in the absence of furin.

Conclusion

The administration of Kurozu-M inhibited tumor growth in a Lovo cell–transplanted mouse model and also inhibited nitrotyrosine production and activation of MMP-2 and MMP-9.

References

[1] Shimoji Y, Tamura Y, Nakamura Y, Nanda K, Nishidai S, Nishikawa Y, et al. Isolation and identification of DPPH radical scavenging compounds in Kurosu (Japanese unpolished rice vinegar). J Agric Food Chem 2002;50:6501–3.

[2] Shen X, Falzon M. PTH-related protein enhances LoVo colon cancer cell proliferation, adhesion, and integrin expression. Regul Pept 2005; 125:17–27.

[3] Shimoji Y, Kohno H, Nanda K, Nishikawa Y, Ohigashi H, Uenakai K, et al. Extract of Kurosu, a vinegar from unpolished rice, inhibits azoxymethane-induced colon carcinogenesis in male F344 rats. Nutr Cancer 2004;49:170–3.

[4] Nanda K, Miyoshi N, Nakamura Y, Shimoji Y, Tamura Y, Nishikawa Y, et al. Extract of vinegar "Kurosu" from unpolished rice inhibits the proliferation of human cancer cells. J Exp Clin Cancer Res 2004;23: 69–75.

[5] Szaleczky E, Pronai L, Nakazawa H, Tulassay Z. Evidence of in vivo peroxynitrite formation in patients with colorectal carcinoma, higher plasma nitrate/nitrite levels, and lower protection against oxygen free radicals. J Clin Gastroenterol 2000;30:47–51.

[6] Shimoji Y, Sugie S, Kohno H, Tanaka T, Nanda K, Tamura Y, et al. Extract of vinegar "Kurosu" from unpolished rice inhibits the development of colonic aberrant crypt foci induced by azoxymethane. J Exp Clin Cancer Res 2003;22:591–7.

[7] Eiserich JP, Hristova M, Cross CE, Jones AD, Freeman BA, Halliwell B, et al. Formation of nitric oxide-derived inflammatory oxidants by myeloperoxidase in neutrophils. Nature 1998;391:393–7.

[8] Fukuyama N, Takebayashi Y, Hida M, Ishida H, Ichimori K, Nakazawa H. Clinical evidence of peroxynitrite formation in chronic renal failure patients with septic shock. Free Radic Biol Med 1997; 22:771–4.

[9] Gullu IH, Kurdoglu M, Akalin I. The relation of gelatinase (MMP-2 and -9) expression with distant site metastasis and tumour aggressiveness in colorectal cancer. Br J Cancer 2000;82:249.

[10] Djonov V, Cresto N, Aebersold DM, Burri PH, Altermatt HJ, Hristic M, et al. Tumor cell specific expression of MMP-2 correlates

with tumor vascularisation in breast cancer. Int J Oncol 2002; 21:25–30.

[11] Steinbrenner H, Ramos MC, Stuhlmann D, Mitic D, Sies H, Brenneisen P. Tumor promoter TPA stimulates MMP-9 secretion from human keratinocytes by activation of superoxide-producing NADPH oxidase. Free Radic Res 2005;39:245–53.

[12] Wittrant Y, Theoleyre S, Couillaud S, Dunstan C, Heymann D, Redini F. Relevance of an in vitro osteoclastogenesis system to study receptor activator of NF-kB ligand and osteoprotegerin biological activities. Exp Cell Res 2004;293:292–301.

[13] Munoz-Najar UM, Neurath KM, Vumbaca F, Claffey KP. Hypoxia stimulates breast carcinoma cell invasion through MT1-MMP and MMP-2 activation. Oncogene 2005.

[14] Migita K, Maeda Y, Abiru S, Komori A, Yokoyama T, Takii Y, et al. Peroxynitrite-mediated matrix metalloproteinase-2 activation in human hepatic stellate cells. FEBS Lett 2005;579:3119–25.

[15] Deryugina EI, Ratnikov BI, Yu Q, Baciu PC, Rozanov DV, Strongin AY. Prointegrin maturation follows rapid trafficking and processing of MT1-MMP in Furin-negative colon carcinoma LoVo cells. Traffic 2004;5:627–41.

Basic Res Cardiol 102:209–216 (2007)
DOI 10.1007/s00395-006-0629-9

ORIGINAL CONTRIBUTION

Naoto Fukuyama
Etsuro Tanaka
Yasuhiko Tabata
Hisanori Fujikura
Masao Hagihara
Hiromi Sakamoto
Kiyoshi Ando
Hiroe Nakazawa
Hidezo Mori

Intravenous injection of phagocytes transfected ex vivo with FGF4 DNA/ biodegradable gelatin complex promotes angiogenesis in a rat myocardial ischemia/reperfusion injury model

Received: 18 April 2006
Returned for 1. revision: 21 June 2006
1. Revision received: 11 September 2006
Accepted: 9 October 2006
Published online: 27 October 2006

N. Fukuyama (✉) · H. Fujikura · M. Hagihara · K. Ando · H. Nakazawa
Depts. of Physiology, Internal Medicine and Center for Regenerative Medicine
Tokai University School of Medicine
Isehara, 259-1193, Japan
Tel.: +81-463/93-1121
Fax: +81-463/93-6684
E-Mail: fukuyama@is.icc.u-tokai.ac.jp

E. Tanaka
Dept. of Nutritional Sciences
Tokyo University of Agriculture
Tokyo, Japan

Y. Tabata
Research Center for Biomedical Engineering
Kyoto University
Kyoto, Japan

H. Sakamoto
Genetics Division
National Cancer Center Research Institute
Tokyo, Japan

H. Mori
National Cardiovascular Center Research Institute
Suita, Japan

Abstract Conventional gene therapies still present difficulties due to poor tissue-targeting, invasiveness of delivery, method, or the use of viral vectors. To establish the feasibility of using non-virally ex vivo transfected phagocytes to promote angiogenesis in ischemic myocardium, gene-transfection into isolated phagocytes was performed by culture with positively charged gelatin impregnated with plasmid DNA. A high rate of gene transfection was achieved in rat macrophages and human monocytes, but not in mouse fibroblasts. The efficiency was 68 ± 11 % in rat macrophages and 78 ± 8 % in human monocytes. Intravenously injected phagocytes accumulated predominantly in ischemic tissue (13 ± 8 %) and spleen (84 ± 6 %), but negligibly in other organs in rodents. The efficiency of accumulation in the target ischemic tissue reached more than 86 % on direct local tissue injection. In a rat model of myocardial ischemia-reperfusion, intravenous injection of fibroblast growth factor 4 (FGF4)-gene-transfected macrophages significantly increased regional blood flow in the ischemic myocardium (78 ± 7.1 % in terms of flow ratio of ischemic/non-ischemic myocardium) compared with intravenous administration of saline (36 ± 11 %) or non-transfected macrophages (42 ± 12 %), or intramuscular administration of naked DNA encoding FGF4 (75 ± 18 %). Enhanced angiogenesis in the ischemic tissue we confirmed histologically. Similarly, intravenous injection of FGF4-gene-transfected monocytes enhanced regional blood flow in an ischemic hindlimb model in mice (93 ± 22 %), being superior to the three other treatments described above (38 ± 12, 39 ± 15, and 55 ± 12 %, respectively).

Phagocytes transfected ex vivo with FGF4 DNA/gelatin promoted angiogenesis. This approach might have potential for non-viral angiogenic gene therapy.

Key words angiogenesis – cells – gene therapy – growth substances – ischemia

Abbreviations and acronyms

ANOVA = analysis of variance
FGF4 = fibroblast growth factor-4
GFP = green fluorescent protein
pI = isoelectric point

Introduction

Conventional gene therapies still require improvement with regard to transfection efficiency and safety [1, 2], as well as tissue targeting [3], despite recent advances. Achievement of a high transfection rate often requires a viral vector, but the safety of the viruses has not yet been

BRC 629

Basic Research in Cardiology, Vol. 102, No. 3 (2007)

established [4–6]. Conventional non-viral vectors seem to be inferior to viral ones in transfection efficiency, except for nucleofection [7, 8]. Conventional gene therapy using a viral vector can induce inflammation in the gene-transduced tissue [9]. Moreover, in vivo gene-delivery to the localized target tissue usually necessitates invasive approaches. For example, direct gene-transfection to cardiomyocytes requires surgical operation [10] or cardiac catheterization [11, 12]. On the other hand, ex vivo gene-transfection is less invasive, but tissue-targeting by intravenous injection is difficult to achieve [3].

Macrophages accumulate in ischemic tissue based on the mechanism of immune response (chemotaxis) [13]. This suggests that intravenous transplantation of macrophages may target the ischemic tissue in vivo. Tabata et al. previously reported that gelatin particles are phagocytized by macrophages [14, 15]. The isoelectric point (pI) of gelatin can be changed by modification of its residues, and positively charged gelatin can be impregnated with negatively charged substances [16] such as nucleic acid [17]. Thus, gelatin may be suitable as a vector for transfecting phagocytes ex vivo.

We describe here a study aimed at examining the feasibility of a new concept for less invasive, cell-based gene therapy, by means of ex vivo gene transfection into isolated phagocytes (macrophages and monocytes) using a non-viral vector, gelatin, followed by intravenous injection of the transfected phagocytes. The present method has significant advantages over conventional cell-based gene delivery [18, 19], in that the intravenously injected cells (phagocytes) not only produce protein from the transfected gene, but have a tissue-targeting ability.

Methods

This study was performed in accordance with the Guideline of Tokai University School of Medicine on Animal Use, which conforms to the NIH Guide for the Care and Use of Laboratory Animals (DHEW publication No. (NIH) 86-23, Revised 1985, Offices of Science and Health Reports, DRR/NIH, Bethesda, MD 20205).

Animals

A total of 121 Fisher rats (male, 10 weeks old, Clea Japan Inc., Tokyo) and 61 nude SCID mice (male, 6 weeks old, Shizuoka Animal Center, Shizuoka, Japan) were used. Rats were anesthetized by inhalation of diethyl ether for harvesting macrophages and with isofluren (1.5–3%) for thoracotomy, after which they were mechanically ventilated with a mixture of oxygen and nitrous oxide. Mice were anesthetized by intraperitoneal injection of sodium pentobarbital (40 mg/kg).

A model of myocardial ischemia-reperfusion injury was prepared in 41 rats. The remaining 80 rats were used for collecting activated macrophages. The heart was exposed via thoracotomy, and the proximal left anterior descending coronary artery was ligated [20] for 180 min, followed by reperfusion. A model of hindlimb ischemia was prepared in 61 mice. The left femoral artery was ligated and resected [21].

Cells

Macrophages were obtained from 80 rats. Thioglycolate (4%, 8 ml) was injected into the peritoneal cavity, and after 4 days, peritoneal macrophages were collected [22]. Monocytes were obtained from peripheral blood of healthy volunteers. Leukocyte-rich plasma was obtained by dextran 500 sedimentation and layered onto Nycoprep 1.068 (Nycomed, Birmingham, UK). The monocyte-containing layer was aspirated, washed twice and allowed to adhere to the dish for 90 minutes. Fibroblasts (NIH 3T3, Invitrogen Corporation, Carlsbad, CA) were also used. The cells were resuspended in RPMI 1640 medium (Sigma) containing 5% heat-inactivated fetal calf serum and cultured for 7–14 days. The cell viability and type were determined by trypan blue exclusion and by immunostaining using anti-macrophage antibody up to 14 days.

Genes and vector

Complementary DNA (cDNA) of green fluorescent protein (GFP), Renilla luciferase or human hst1/FGF4 (FGF4) [17] was inserted into the expression vector pRC/CMV (Invitrogen Corporation, Carlsbad, CA) and the constructs were designated as pRC/CMV-GFP, pRC/CMV-luciferase and pRC/CMV-HST1-10, respectively. Preparation and purification of the plasmid from cultures of pRC/CMV-GFP-, pRC/CMV-luciferase-, or pRC/CMV-HST1-10-transformed *Escherichia coli* were performed by equilibrium centrifugation in cesium chloride-ethidium bromide gradients.

Gelatin was prepared from porcine skin [14]. After swelling in water the gelatin particles used in this study were spheroids with a diameter of approximately 5–30 μm, water content of 95%, and pI of 11. Gelatin (2 mg) was incubated with 50 μg of the plasmid for 7 days at 4 °C to make a gelatin-DNA complex [14].

Experimental protocols

Ex vivo gene transfection Macrophages, monocytes, and fibroblasts (1×10^6) were cultured with the gelatin-DNA complex (2 mg of gelatin plus 50 μg of DNA) for 14 days on a culture dish (100 mm in diameter). Gene ex-

pression of GFP was evaluated by fluorescence microscopy and fluorescence-activated cell sorting. Luciferase activity in the cell lysate was evaluated with a photon counter system after cell lysis [23].

Organ distribution of phagocytes injected intravenously and directly into ischemic muscle To examine tissue-targeting by intravenous injection of transfected phagocytes, the distribution of the cells into organs was evaluated by immunohistochemistry. In the rat model of myocardial ischemia-reperfusion injury, the GFP-gene-transfected macrophages (1.0×10^6 each) were injected into the superficial dorsal vein of the penis at the initiation of reperfusion (n = 7 and 5, respectively). In the mouse model of hindlimb ischemia, the GFP-gene-transfected monocytes (1.0×10^6) were injected into the caudal vein 14 days after induction of ischemia (n = 5). To examine the tissue-targeting by direct local injection of transfected phagocytes, the distribution of the cells into organs was also evaluated. In the rat model of myocardial ischemia-reperfusion injury (n = 7) and the mouse model of hindlimb ischemia (n = 5), the same numbers of transfected macrophages and monocytes were directly injected into ischemic myocardium and ischemic skeletal muscle, respectively. Tissue samples were obtained 24 hours after cell administration. Each tissue was homogenized and cytospin was performed. Immunohistochemical analysis was done with anti-GFP antibody (CLONTECH, USA. GFP-monoclonal antibody). GFP positive macrophages were counted in each tissue and expressed as a percentage of total GFP-positive cells.

Amelioration of ischemia by intravenous injection of angiogenic gene-transfected phagocytes The angiogenic effect of intravenously injected FGF4-gene-transfected phagocytes on the ischemia models was evaluated. In the rat model of myocardial ischemia-reperfusion injury, FGF4-gene-transfected macrophages (n = 5), non-transfected macrophages (1.0×10^6 each) (n = 5), or saline (n = 5) were injected into the superficial dorsal vein of the penis, or naked FGF4-DNA (50 μg) was injected directly into the ischemic myocardium (n = 5), at the initiation of reperfusion. Fourteen days after the cell administration, blood flows in the ischemic and non-ischemic regions in the heart were evaluated with a non-contact laser Doppler flowmeter (FLO-N1, Omegawave Corporation). Then, tissue samples were obtained and histological analysis was performed. In a mouse model of hindlimb ischemia, just after induction of ischemia, FGF4-gene-transfected monocytes (n = 15), non-transfected monocytes (n = 8) (1.0×10^6 each), or saline (n = 10) were injected into the caudal vein, or naked FGF4-DNA (50 μg) was injected directly into the ischemic muscle (n = 12). Fourteen days after induction of ischemia, blood flows in the limbs were evaluated with the noncontact laser Doppler flowmeter (FLO-N1, Omegawave Corporation).

Histology

Ten micrometer sections were cut from formalin-fixed, paraffin-embedded tissue. Two sections were used for H.E. staining and azan staining, and eight sections were used for immunohistochemical staining. Immunohistochemical staining was performed by an indirect immunoperoxidase method. Anti-GFP antibody, anti-Mac1 antibody (BMA Biomedicals Ag, Switzerland), and anti-CD31 antibody (Serotec, UK) were used as primary antibodies. Mac1-antigen is specific to macrophages/monocytes. Anti-Ig, peroxidase-linked species-specific F(ab')2 fragments (Amersham Pharmacia Biotech UK Ltd., UK), were used as a secondary antibody. Double staining was performed with alkaline staining and peroxidase staining. The vessel density stained with von Willebrand factor-antibody was calculated by morphometric assessment in one 16 randomly selected fields of each heart and expressed as number/mm^2.

Statistical analysis

Data are presented as mean values ± SD. Differences were assessed by using ANOVA (analysis of variance) with the Scheffe's multiple comparisons test. A value of $P < 0.05$ was considered statistically significant.

Results

Ex vivo gene transfection

We studied whether genes could be transfected into isolated rat macrophages, human monocytes, and mouse fibroblasts ex vivo by using gelatin. Transfection of the GFP gene into isolated rat macrophages (Figs. 1A and B) and human monocytes (Figs. 1C and D), but not into mouse fibroblasts (data not shown), was achieved by culture with gelatin-DNA complex for 14 days. The gene transfection efficiency into rat macrophages was 68 ± 11 % (30 experiments, Fig. 2A) and that into human monocytes was 78 ± 8 % (30 experiments) as determined with a fluorescence activated cell sorter. Sequential analysis after luciferase-gene transfection into rat macrophages revealed high expression after 14 days of culture (Fig. 2B).

Basic Research in Cardiology, Vol. 102, No. 3 (2007)

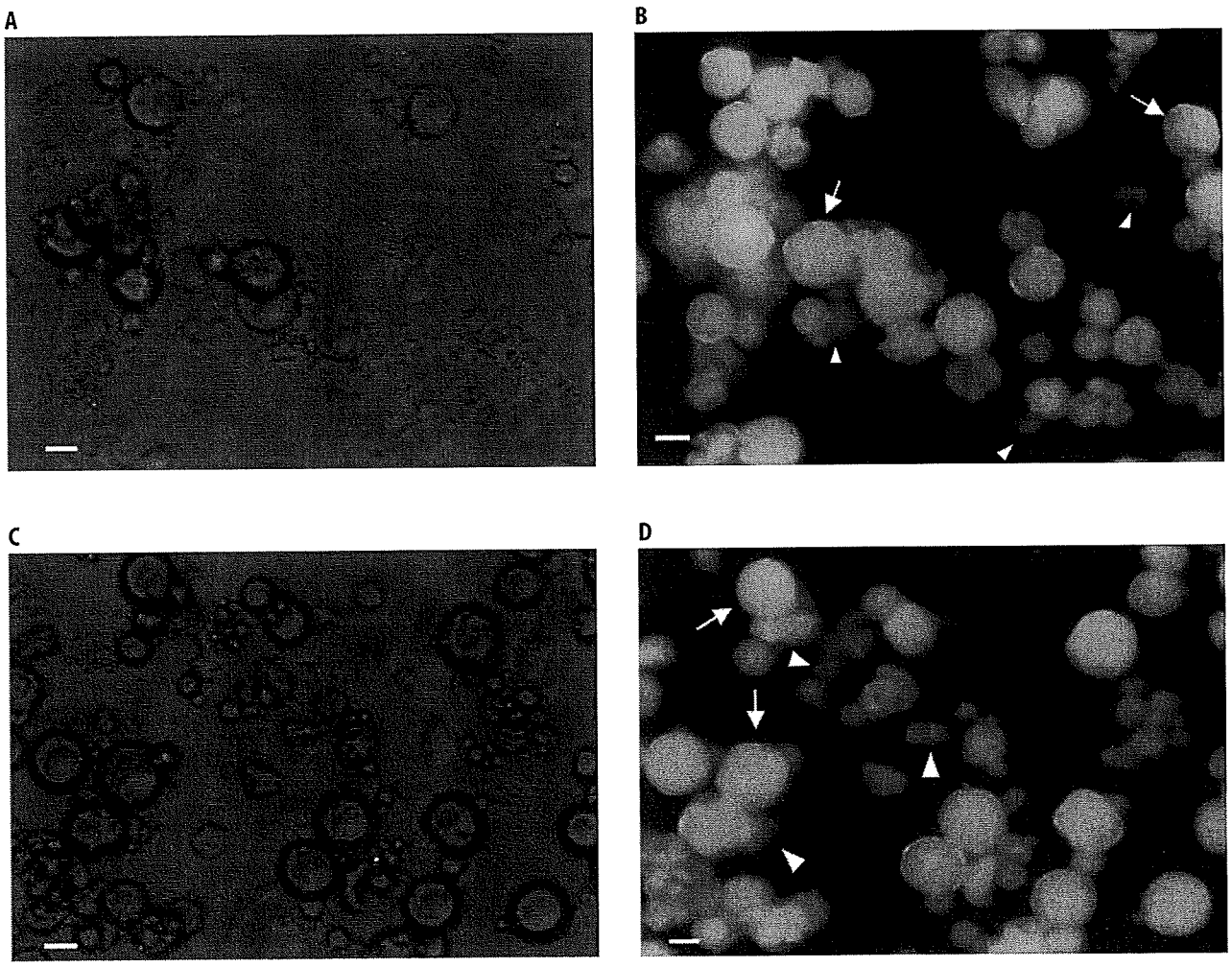

Fig. 1 Fluorescent presentation of ex vivo gene transfection with gelatin-DNA complex in macrophages/monocytes as well as fibroblasts. Rat macrophages (**A** and **B**) and human monocytes (**C** and **D**) were cultured with gelatin-GFP-gene complex for 14 days. Transmittance microscopic images (**A** and **C**) and fluorescence images (**B** and **D**) of the cells are shown. Macrophages (**B**) and monocytes (**D**) show fluorescence due to GFP. Arrowheads indicate GFP-expressing cells. Arrows indicate gelatin particles themselves. Bars = 20 μm

Organ distribution of phagocytes injected intravenously or directly into ischemic muscle

We studied quantitatively whether intravenously injected luciferase-gene-transfected phagocytes could target ischemic tissues (the third and fifth columns from the left in Table 1). In non-ischemic rats, the injected macrophages were recognized almost exclusively in the spleen (98 ± 4 %) (n = 7, the second column in Table 1). In non-ischemic mice, similar results were observed (n = 7, data not shown). In a rat with myocardial ischemia-reperfusion injury, some of the intravenously injected macrophages were incorporated into the heart (the third column in Table 1). The incorporation into the post-ischemic pericardium amounted to 13 ± 6 % (n = 7) (non-ischemic rats 0 ± 0 %, n = 7, Table 1). The incorporated cells expressed GFP (Fig. 3). Fibrosis with inflammatory infiltrates was recognized in the anterior wall of the left ventricle, extending to the interventricular septum (Figs. 3A and B). These infiltrates were mainly polymorphonuclear leukocytes and macrophages (Figs. 3C and D). Approximately 20 % of the macrophages showed GFP-positivity in this area (Figs. 3E and F). Similar tissue-targeting by intravenously injected monocytes was confirmed in a mouse model with hindlimb ischemia (13 ± 7 %, n = 7, the fifth column in Table 1). Furthermore, we studied whether local intramuscular injection increased the degree of tissue targeting (the fourth and sixth columns from the left in Table 1). After direct injection of phagocytes into ischemic muscle, 86 ± 10 % and 88 ± 6 % of the cells remained in the target tissue in the two models. Thirteen and 11 % of phagocytes in-

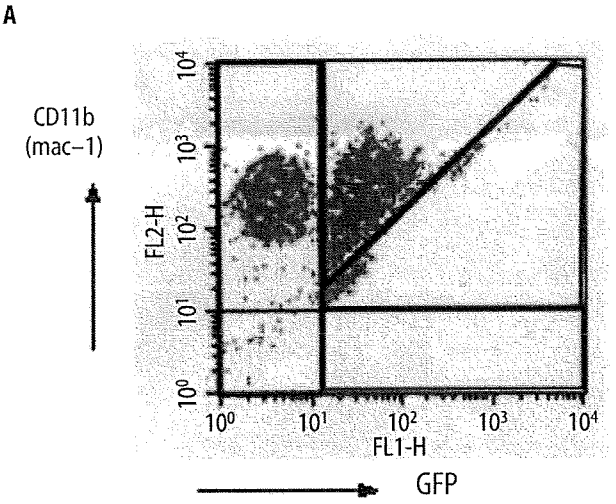

Fig. 2 Quantitative assessment of gene transfection into rat macrophages. (**A**) Fluorescence-activated cell sorting analysis of transfected macrophages done on day 14 of culture with reference to GFP-positive and Mac1-positive cells. (**B**) Sequential changes of luciferase activity in cultured macrophages in the presence of luciferase-gene-gelatin complex. Values are mean ± SD. The number of experiments is shown in parentheses

jected into the cardiac or hindlimb muscle migrated to the spleen. In the other organs, accumulation of phagocytes were negligible.

Amelioration of ischemia by intravenously injected angiogenic-gene-transfected phagocytes

In the rat model with myocardial ischemia-reperfusion injury, we studied the angiogenic effect of intravenously injected macrophages transfected with fibroblast growth factor 4 (FGF4) gene by using gelatin. Intravenous injection of these macrophages (1.0×10^6) significantly increased the regional blood flow in the ischemic myocardium (78 ± 7.1 %, n = 8, in terms of flow ratio of ischemic/non-ischemic myocardium) compared with the other three treatments ($P < 0.05$, ANOVA), that is, intravenous administration of saline (35 ± 10 %, n = 8), intramuscular administration of naked DNA encoding FGF4 (50 μg, direct intramyocardial injection after thoracotomy) (58 ± 5.3 %, n = 8), and intravenous administration of the same number of non-transfected macrophages (42 ± 12 %, n = 8) (Fig. 4A). Histological analyses revealed angiogenesis in the ischemic tissue after the administration of transfected cells (Figs. 4B and C). Similar results were observed in the mouse model with hindlimb ischemia. Intravenous injection of FGF4-gene-transfected monocytes (1.0×10^6) enhanced regional blood flow in the ischemic leg (Fig. 4D). The increase of blood flow in the mice with transfected monocytes (93 ± 22 % in terms of flow ratio of ischemic/non-ischemic leg) was significantly larger than those obtained with the other three treatments described above (38 ± 12, 55 ± 12, and 39 ± 15 %, $P < 0.05$, ANOVA). Neither lymph node swelling in any part of the body nor pathologic change in the spleen or lung, such as angioma or abnormal immune response, was found in any of the animals.

Table 1 Organ distribution of phagocytes injected into the vein and into local tissue

Organ	Normal i.v. (7 rats)	Myocardial injury i.v. (7 rats)	Myocardial injury i.m. (7 rats)	Hindlimb ischemia i.v. (7 mice)	Hindlimb ischemia i.m. (7 mice)
Heart	0 ± 0	13 ± 6	86 ± 10	0 ± 0	0 ± 0
Hindlimb muscle	0 ± 0	0 ± 0	0 ± 0	13 ± 7	88 ± 6
Spleen	98 ± 4	84 ± 6	13 ± 10	84 ± 6	11 ± 6
Lung	1 ± 2	1 ± 1	1 ± 2	1 ± 2	1 ± 1
Liver	1 ± 2	1 ± 1	1 ± 1	1 ± 2	1 ± 1
Brain	0 ± 0	0 ± 0	0 ± 0	0 ± 0	0 ± 0
Kidney	0 ± 0	0 ± 0	0 ± 0	0 ± 0	0 ± 0
Intestine	0 ± 0	0 ± 0	0 ± 0	0 ± 0	0 ± 0

Each value shows a distribution ratio (%) into organs of transfected macrophages/monocytes (mean ± SD). *i.v.* intravenous injection into the vein; *i.m.* direct injection into the jeopardized muscle

Discussion

The advantages of the present method are as follows. First, genes can easily be transfected into phagocytes (macrophages/monocytes). In preliminary experiments, we found that genes can also be transfected into endothelial progenitor cells [25]. Compared with other transfection method, the transfection efficiency was high (68 ± 11 %) and it is not necessary to use a potentially hazardous viral vector [2, 26, 32]. Second, the phagocytes can target the pathologic tissues by chemotaxis even after intravenous injection, and higher tar-

Basic Research in Cardiology, Vol. 102, No. 3 (2007)

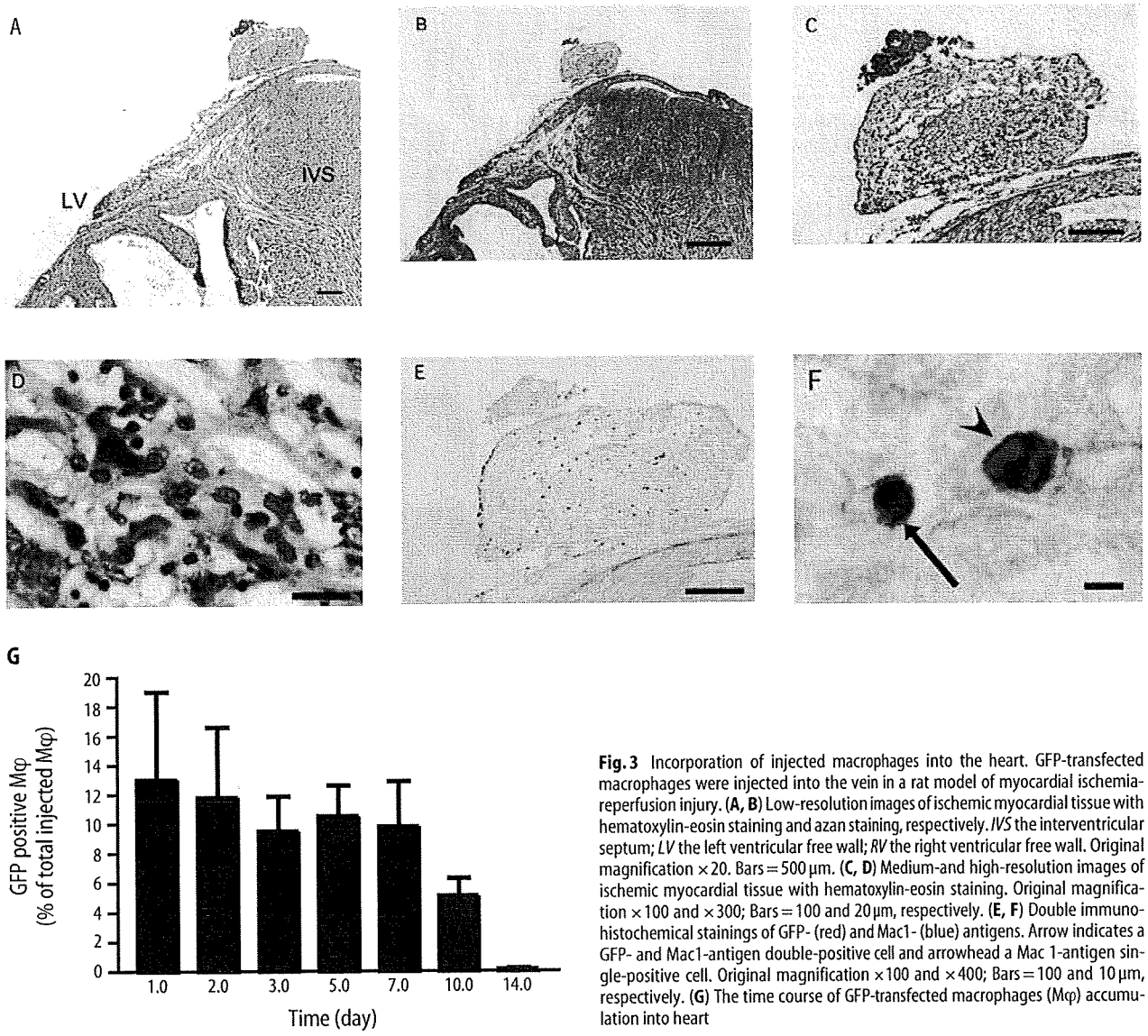

Fig. 3 Incorporation of injected macrophages into the heart. GFP-transfected macrophages were injected into the vein in a rat model of myocardial ischemia-reperfusion injury. **(A, B)** Low-resolution images of ischemic myocardial tissue with hematoxylin-eosin staining and azan staining, respectively. *IVS* the interventricular septum; *LV* the left ventricular free wall; *RV* the right ventricular free wall. Original magnification ×20. Bars = 500 μm. **(C, D)** Medium-and high-resolution images of ischemic myocardial tissue with hematoxylin-eosin staining. Original magnification ×100 and ×300; Bars = 100 and 20 μm, respectively. **(E, F)** Double immunohistochemical stainings of GFP- (red) and Mac1- (blue) antigens. Arrow indicates a GFP- and Mac1-antigen double-positive cell and arrowhead a Mac 1-antigen single-positive cell. Original magnification ×100 and ×400; Bars = 100 and 10 μm, respectively. **(G)** The time course of GFP-transfected macrophages (Mφ) accumulation into heart

geting is available if they are administered locally. The injection is repeatable. We confirmed that the angiogenic gene-transfected phagocytes enhanced angiogenesis after ischemia-reperfusion injury in rat heart and ameliorated ischemia in a mouse hindlimb model.

The injected phagocytes migrated into pathologic tissues, presumably in response to the release of cytokines such as monocyte chemoattractant protein 1 by injured endothelial cells [27]. Adhesion molecules such as P-selectin [28] are probably involved in the recruitment of phagocytes to the vessel wall. The injected phagocytes also migrated to the spleen, but no pathologic change was found in the spleen.

The present method has several advantages over conventional methods of cell-based gene therapy such as fibroblast-based and smooth muscle cell-based approaches [18, 19, 33, 34]. For example, monocytes do not aggregate in vessels, while fibroblasts or smooth muscle cells cannot be injected intravenously because of aggregation. The transfected phagocytes not only synthesize protein from the transfected gene, but also are partially targeted to the impaired tissue. In addition, the transfection rate was better than those of methods such as lipofection, viral vectors and electroporation [26, 29]. The newly developed technique of nucleofection has a transfection efficiency of 40–70 % [30], which is similar to that of our method, but our procedure is easier to use [30, 31]. Further, the therapeutic effect obtained here was superior to that of conventional gene therapy which we reported previously, i.e., intramuscular injection of

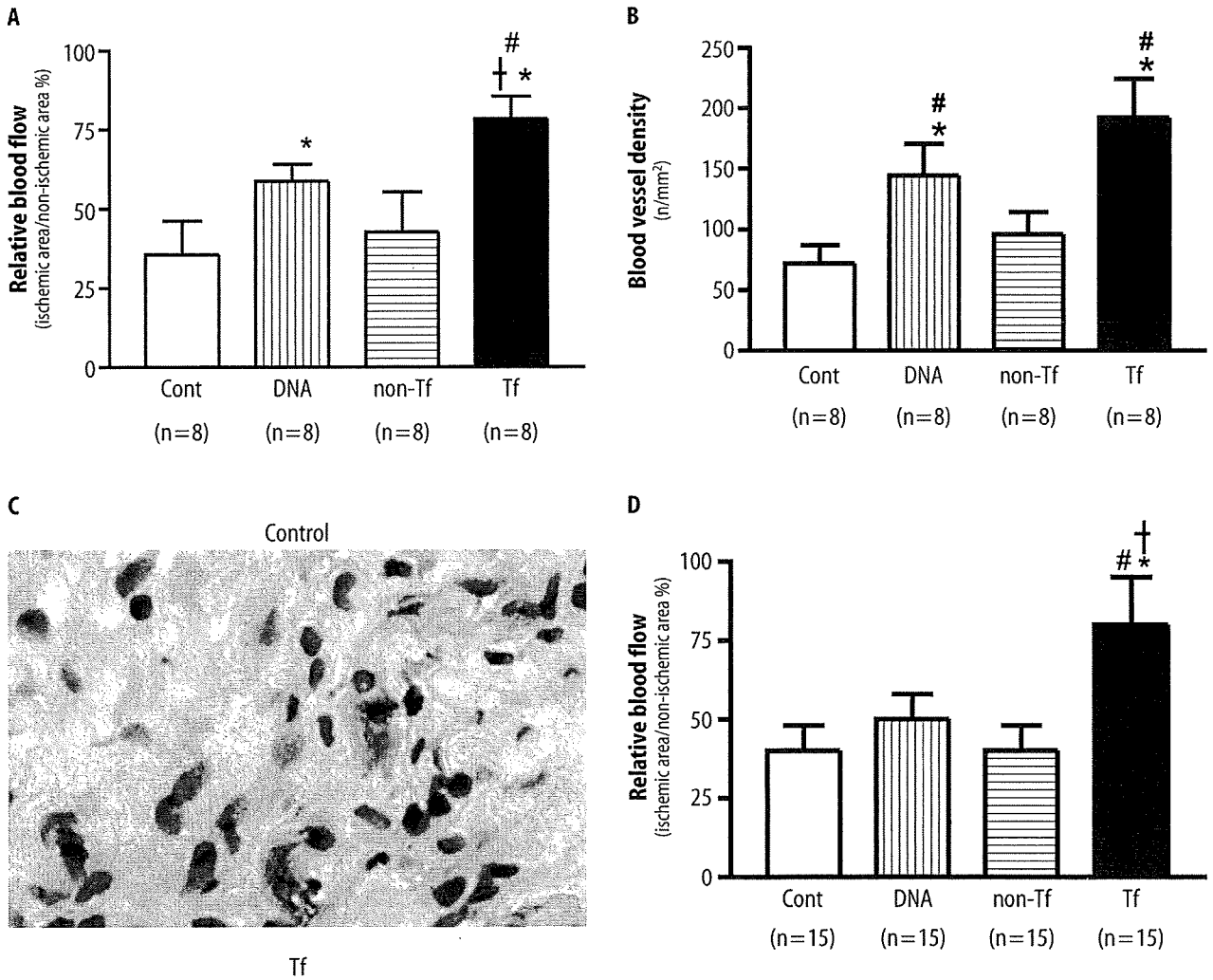

Fig. 4 Therapeutic effects of angiogenic-gene-transfected phagocytes on ischemia. FGF4-transfected macrophages were injected into the vein or naked DNA encoding FGF4 was injected directly into the myocardium in a rat model of myocardial ischemia-reperfusion injury (**A–C**). FGF4-transfected monocytes were injected into the vein or naked DNA encoding FGF4 was injected directly into the ischemic muscle in a mouse model of hindlimb ischemia (**D**). (**A**) Relative blood flow in the ischemic myocardium. Each flow represents a relative value with respect to non-ischemic region. The number of animals is shown in parentheses. (**B**) Quantification of vessel density in the ischemic myocardium. The number of observation fields is shown in parentheses. (**C**) Immunohistochemical staining in the ischemic myocardium with anti-CD31 antibody. (**D**) Relative blood flow in the ischemic leg. Each flow represents a relative value with respect to non-ischemic leg. The number of animals is shown in parentheses. Control represents animals injected with saline into the vein; *DNA* naked DNA encoding FGF4 was injected directly into the ischemic muscle; *non-Tf* non-transfected phagocytes were injected intravenously, *Tf* FGF4-gene-transfected phagocytes were injected intravenously. Values are mean ± SD. $P < 0.05$ vs *Cont, †DNA, and #non-Tf (ANOVA)

naked DNA, in ischemia models of heart and leg [17]. The major disadvantage of our method is the cell preparation time of 2 weeks before therapy can be started, and further work is needed to speed up this process.

Acknowledgements The authors wish to thank Jobu Itoh, Yoshiko Shinozaki, and Takayuki Hasegawa for their technical work.

References

1. Pfeifer A, Verma IM (2001) Gene therapy: promises and problems. Annu Rev Genomics Hum Genet 2:177–211
2. Watson DJ, Kobinger GP, Passini MA, Wilson JM, Wolfe JH (2002) Targeted transduction patterns in the mouse brain by lentivirus vectors pseudotyped with VSV, Ebola, Mokola, LCMV, or MuLV envelope proteins. Mol Ther 5:528–537
3. Li Q, Bolli R, Qiu Y, Tang XL, Guo Y, French BA (2001) Gene therapy with extracellular superoxide dismutase protects conscious rabbits against myocardial infarction. Circulation 103: 1893–1898
4. Ferber D (2001) Gene therapy. Safer and virus-free? Science 294:1638–1642
5. Kay MA, Glorioso JC, Naldini L (2001) Viral vectors for gene therapy: the art of turning infectious agents into vehicles of therapeutics. Nat Med 7:33–40
6. Isner JM (2002) Myocardial gene therapy. Nature 415:234–239
7. Nishikawa M, Hashida M (2002) Nonviral approaches satisfying various requirements for effective in vivo gene therapy. Biol Pharm Bull 25:275–283
8. Schakowski F, Buttgereit P, Mazur M, Mazur M, Marten A, Schottker B, Gorschluter M, Schmidt-Wolf IG (2004) Novel non-viral method for transfection of primary leukemia cells and cell lines. Genet Vaccines Ther 2:1
9. Tomasoni S, Benigni A (2004) Gene therapy: how to target the kidney. Promises and pitfalls. Curr Gene Ther 4: 115–122
10. Losordo DW, Vale PR, Symes JF, Dunnington CH, Esakof DD, Maysky M, Ashare AB, Lathi K, Isner JM (1998) Gene therapy for myocardial angiogenesis: initial clinical results with direct myocardial injection of phVEGF165 as sole therapy for myocardial ischemia. Circulation 98:2800–2804
11. Kornowski R, Leon MB, Fuchs S, Vodovotz Y, Flynn MA, Gordon DA, Pierre A, Kovesdi I, Keiser JA, Epstein SE (2000) Electromagnetic guidance for catheter-based transendocardial injection: a platform for intramyocardial angiogenesis therapy. Results in normal and ischemic porcine models. J Am Coll Cardiol 35:1031–1039
12. Laitinen M, Hartikainen J, Hiltunen MO, Eranen J, Kiviniemi M, Narvanen O, Makinen K, Manninen H, Syvanne M, Martin JF, Laakso M, Yla-Herttuala S (2000) Catheter-mediated vascular endothelial growth factor gene transfer to human coronary arteries after angioplasty. Hum Gene Ther 11:263–270
13. Ramsay SC, Weiller C, Myers R, Cremer JE, Luthra SK, Lammertsma AA, Frackowiak RS (1992) Monitoring by PET of macrophage accumulation in brain after ischaemic stroke. Lancet 339:1054–1055
14. Tabata Y, Ikada Y (1987) Macrophage activation through phagocytosis of muramyl dipeptide encapsulated in gelatin microspheres. J Pharm Pharmacol 39: 698–704
15. Tabata Y, Ikada Y (1988) Macrophage phagocytosis of biodegradable microspheres composed of L-lactic acid/glycolic acid homo- and copolymers. J Biomed Mater Res 22:837–858
16. Ikada Y, Tabata Y (1998) Protein release from gelatin matrices. Adv Drug Deliv Rev 31:287–301
17. Kasahara H, Tanaka E, Fukuyama N, Sato E, Sakamoto H, Tabata Y, Ando K, Iseki H, Shinozaki Y, Kimura K, Kuwabara E, Koide S, Nakazawa H, Mori H (2003) Biodegradable gelatin hydrogel potentiates the angiogenic effect of fibroblast growth factor 4 plasmid in rabbit hindlimb ischemia. J Am Coll Cardiol 41:1056–1062
18. Xie Y, Yang ST, Kniss DA (2001) Three-dimensional cell-scaffold constructs promote efficient gene transfection: implications for cell-based gene therapy. Tissue Eng 7:585–598
19. Panetta CJ, Miyauchi K, Berry D, Simari RD, Holmes DR, Schwartz RS, Caplice NM (2002) A tissue-engineered stent for cell-based vascular gene transfer. Hum Gene Ther 13:433–441
20. Gidh-Jain M, Huang B, Jain P, el-Sherif N (1996) Differential expression of voltage-gated K+ channel genes in left ventricular remodeled myocardium after experimental myocardial infarction. Circ Res 79:669–675
21. Takeshita S, Zheng LP, Brogi E, Kearney M, Pu LQ, Bunting S, Ferrara N, Symes JF, Isner JM (1994) Therapeutic angiogenesis. A single intraarterial bolus of vascular endothelial growth factor augments revascularization in a rabbit ischemic hind limb model. J Clin Invest 93:662–670
22. Ribeiro RA, Flores CA, Cunha FQ, Ferreira SH (1991) IL-8 causes in vivo neutrophil migration by a cell-dependent mechanism. Immunology 73:472–477
23. Fukuyama N, Ichimori K, Su Z, Ishida H, Nakazawa H (1996) Peroxynitrite formation from activated human leukocytes. Biochem Biophys Res Commun 224:414–419
24. Mori H, Haruyama S, Shinozaki Y, Okino H, Iida A, Takanashi R, Sakuma I, Husseini WK, Payne BD, Hoffman JI (1992) New nonradioactive microspheres and more sensitive X-ray fluorescence to measure regional blood flow. Am J Physiol 263:H1946–H1957
25. Nagaya N, Kangawa K, Kanda M, Uematsu M, Horio T, Fukuyama N, Hino J, Harada-Shiba M, Okumura H, Tabata Y, Mochizuki N, Chiba Y, Nishioka K, Miyatake K, Asahara T, Hara H, Mori H (2003) Hybrid cell-gene therapy for pulmonary hypertension based on phagocytosing action of endothelial progenitor cells. Circulation 108: 889–895
26. Kobinger GP, Deng S, Louboutin JP, Vatamaniuk M, Matschinsky F, Markmann JF, Raper SE, Wilson JM (2004) Transduction of human islets with pseudotyped lentiviral vectors. Hum Gene Ther 15:211–219
27. Leonard EJ, Yoshimura T (1990) Human monocyte chemoattractant protein-1 (MCP-1). Immunol Today 11:97–101
28. Ikeda Y, Young LH, Lefer AM (2002) Attenuation of neutrophil-mediated myocardial ischemia-reperfusion injury by a calpain inhibitor. Am J Physiol Heart Circ Physiol 282:H1421–H1426
29. Veit K, Boissel JP, Buerke M, Grosser T, Meyer J, Darius H (1999) Highly efficient liposome-mediated gene transfer of inducible nitric oxide synthase in vivo and in vitro in vascular smooth muscle cells. Cardiovasc Res 43:808–822
30. Maasho K, Marusina A, Reynolds NM, Coligan JE, Borrego F (2004) Efficient gene transfer into the human natural killer cell line, NKL, using the Amaxa nucleofection system. J Immunol Methods 284:133–140
31. Mertz KD, Weisheit G, Schilling K, Luers GH (2002) Electroporation of primary neural cultures: a simple method for directed gene transfer in vitro. Histochem Cell Biol 118:501–506
32. Lei Y, Haider HK, Shujia J, Sim ES (2004) Therapeutic angiogenesis; Devising new strategies based on past experiences. Basic Res Cardiol 99:121–132
33. Ott HC, McCue J, Taylor DA (2005) Cell-based cardiovascular repair: The hurdles and the opportunities. Basic Res Cardiol 100:504–517
34. Koch KC, Schaefer WM, Liehn EA, Rammos C, Mueller D, Schroeder J, Dimassi T, Stopinski T, Weber C (2006) Effect of catheter-based transendocardial delivery of stromal cell-derived factor 1α on left ventricular function and perfusion in a porcine model of myocardial infarction. Basic Res Cardiol 101:69–77

FEBS Letters 581 (2007) 2416–2422

Crystal structures of catrocollastatin/VAP2B reveal a dynamic, modular architecture of ADAM/adamalysin/reprolysin family proteins

Tomoko Igarashi[a], Satohiko Araki[b], Hidezo Mori[a], Soichi Takeda[a,*]

[a] *Department of Cardiac Physiology, National Cardiovascular Center Research Institute 5-7-1 Fujishiro-dai, Suita, Osaka 565-8565, Japan*
[b] *Sugashima Marine Biological Laboratory, Graduate School of Science, Nagoya University, Toba, Mie 517-0004, Japan*

Received 26 January 2007; revised 29 March 2007; accepted 20 April 2007

Available online 30 April 2007

Edited by Christian Griesinger

Abstract Catrocollastatin/vascular apoptosis-inducing protein (VAP)2B is a metalloproteinase from *Crotalus atrox* venom, possessing metalloproteinase/disintegrin/cysteine-rich (MDC) domains that bear the typical domain architecture of a disintegrin and metalloproteinase (ADAM)/adamalysin/reprolysin family proteins. Here we describe crystal structures of catrocollastatin/VAP2B in three different crystal forms, representing the first reported crystal structures of a member of the monomeric class of this family of proteins. The overall structures show good agreement with both monomers of atypical homodimeric VAP1. Comparison of the six catrocollastatin/VAP2B monomer structures and the structures of VAP1 reveals a dynamic, modular architecture that may be important for the functions of ADAM/adamalysin/reprolysin family proteins.

Keywords: ADAM; Adamalysin; Reprolysin; MDC protein; Metalloproteinase disintegrin; Apoptotic toxin

1. Introduction

Hemorrhagic snake venoms induce local and systemic hemorrhaging by disrupting the walls of the blood vessels in envenomed patients [1]. In vitro, they induce apoptosis specifically in cultured vascular endothelial cells [2]. Vascular apoptosis-inducing protein (VAP)1 and VAP2 were originally isolated from *Crotalus atrox* venom [3,4], and similar apoptotic toxins have been isolated from other snake venoms [5–7]. VAP1 is a disulfide-bridged homodimeric protein with an apparent molecular weight of 110 kDa, and an isoelectric point of 8.5. VAP2 is a single chain protein with a MW of 55 kDa and an isoelectric point of 4.5 [3,4,8]. VAPs are members of the P-III class of snake venom metalloproteinases (SVMPs), possessing a metalloproteinase/disintegrin/cysteine-rich (MDC) domain architecture typical of a disintegrin and metalloproteinase (ADAM)/adamalysin/reprolysin family proteins [9,10]. VAP-induced apoptosis is dependent on its catalytic activity [8], is inhibited by antibodies to integrins α3, α6, β1 and CD9 [11], and involves activation of specific caspases [12]. However, the physiological targets of VAPs and the underlying mechanism of VAP-induced apoptosis remain elusive.

ADAMs are a family of mammalian membrane-anchored glycoproteins that have been implicated in the processing of cell surface and extracellular matrix proteins [13,14]. The crystal structures of several P-I class SVMPs, which contain only a metalloproteinase (M)-domain, and the isolated M and disintegrin/cysteine-rich (DC) domains of ADAMs have been determined [15–18]. However, structures of ADAM/adamalysin/reprolysin family proteins that include the entire MDC domain have not been determined. The relevance of the multidomain structure to the catalytic and adhesive functions of this family of proteins is an important issue that remains to be elucidated. To better understand the structure–function relationship of ADAM/adamalysin/reprolysin family proteins, and how it relates to the molecular mechanism of VAP-induced apoptosis, we have been engaged in crystallographic studies of VAPs. Recently, we determined the crystal structure of VAP1, revealing the MDC domain architecture for the first time [19]. Although the intrinsic two-fold symmetry of atypical homodimeric VAP1 conferred a great advantage for both its crystallization and structural resolution, the possibility remained that the spatial arrangement of the MDC domains of VAP1 differed from that of monomeric SVMPs and ADAMs, due to crystallographic restraints imposed on the molecule. The majority of ADAMs and SVMPs do not to form VAP1-type dimers, most likely due to the lack of a consensus QDHSK sequence [19] (residues 320–324 in VAP1, in which the Nζ atom of Lys324 is coordinated by the six oxygen atoms of another monomer and plays a pivotal role in dimer formation), and Cys365, which are conserved among the dimeric SVMPs (Supplementary Fig. 1). Therefore, to elucidate the general architecture of proteins of the ADAM/adamalysin/reprolysin family, we crystallized VAP2 and determined its structure. We modeled all of the structures as monomers of VAP2B, which is identical to catrocollastatin, a protein previously isolated as a platelet aggregation inhibitor [20]. Here we describe the structure of catrocollastain/VAP2B, as determined in three different crystal forms. These are the first reported crystal structures of the monomeric class of proteins in ADAM/adamalysin/reprolysin family.

2. Materials and methods

Protein preparation and crystallization were performed as previously described [21]. The diffraction data sets were collected at the

*Corresponding author. Fax: +81 6 6872 7485.
E-mail address: stakeda@ri.ncvc.go.jp (S. Takeda).

Abbreviations: ADAM, a disintegrin and metalloproteinase; MDC, Metalloproteinase/disintegrin/cysteine-rich; SVMP, Snake venom metalloproteinase; HVR, Hyper-variable-region; ncs, Non-crystallographic symmetry; VAP, Vascular apoptosis-inducing protein; PEG, Polyethyleneglycol

0014-5793/$32.00
doi:10.1016/j.febslet.2007.04.057

SPring-8 beamline BL41XU using the ADSC quantum 315 CCD detector with a wavelength of 1.0 Å at 100 K. Images were reduced using HKL2000 [22] (Table 1). Structures were solved using the molecular replacement (MR) method and the MOLREP program of the CCP4 suite [23], with the structure of VAP1 (2ERO) as a starting model. The M- and C-domains of the VAP1 were used separately as the search models. An MR solution was initially obtained from the Form 2-2 crystal data set, which assumed two M-domains and two C-domains in the asymmetric units. After the model was manually rebuilt using TURBO-FRODO [24], it was subjected to torsional molecular dynamic refinements using CNS [25]. Iterative refinements and manual rebuilding of the model improved the electron-density map and enabled us to model the remaining part of the molecule. The composite omit electron-density maps created by CNS were used to confirm the chain tracing. After the polypeptide chains were modeled, we modeled zinc and calcium ions and the inhibitor GM6001 (3-(*N*-hydroxycarboxamide)-2-isobutyl-propanoyl-Trp-methylamide), then the components of the carbohydrate chain linked to Asn371.

The two monoclinic crystal structures were solved by MR with the domains of the refined Form 2-2 crystal structure as a starting model. In all three crystal forms, the asymmetric unit contained two monomers of catrocollastatin/VAP2B. Refinement statistics are shown in Table 1. During the course of our analysis, we found a point mutation (F203V) in the crystallized specimens. By comparing the structures with that of VAP1, which has a phenylalanine at this position, we determined that this mutation does not introduce a large structural change or affect the flexibility of the molecule. Graphical representations were prepared using the programs TURBO-FRODO [24], MOLSCRIPT [26], RASTER3D [27] and PyMOL [28].

3. Results and discussion

3.1. Structural determination

Purified VAP2 was crystallized in variety of forms [21]. In the current study, we determined the structures of three of these crystal forms. Previously, we observed that the VAP2 preparation is a mixture of two homologous polypeptide chains, VAP2A and VAP2B [29]. To identify the molecules in the crystals as either VAP2A or catrocollastatin/VAP2B, we carefully analyzed the composite omit electron-density maps corresponding to the 11 amino acid residues that are distinct between the two proteins (Supplementary Fig. 1). Based on this assessment, the major component in the three crystals was determined to be catrocollastain/VAP2B. Therefore, in the present study, we modeled all six molecules as catrocollastain/VAP2B. The indole ring of GM6001 provided additional

Table 1
Data collection and refinement statistics

	Form 2-1	Form 2-2	Form 2-5
Data collection			
Space group	$P2_1$	$P2_12_12_1$	$C2$
Cell dimensions			
a, *b*, *c* (Å)	56.9, 138.0, 59.2	57.7, 118.2, 138.5	220.7, 79.5, 58.7
a, b, c (°)	90, 91.5, 90	90, 90, 90	90, 91.7, 90
Resolution (Å) (high resolution shell)	50–2.15(2.23–2.15)	50–2.50(2.59–2.50)	50–2.70(2.80–2.70)
No. of unique reflections	48664(4428)	33288(2925)	26911(2313)
[a]R_{merge}	0.081(0.196)	0.089(0.321)	0.085(0.231)
$I/\sigma(I)$	9.8(4.6)	10.3(3.7)	10.1(5.5)
Completeness (%)	98.1(89.5)	98.6(88.4)	95.9(82.5)
Redundancy	3.3(2.0)	6.5(3.3)	3.4(2.8)
Refinement			
Resolution (Å) (high resolution shell)	50–2.15(2.23–2.15)	50–2.50(2.59–2.50)	50–2.70(2.80–2.70)
No. of reflections	48628(4386)	33099(2922)	26907(2276)
[b]R_{work}	0.175(0.195)	0.227(0.316)	0.199(0.264)
[c]R_{free}	0.228(0.277)	0.286(0.399)	0.260(0.328)
Average B-factors (No. of atoms)			
All atoms	19.9(7292)	38.5(6801)	25.1(6823)
Protein	18.5(6422)	38.1(6438)	24.7(6438)
Main chain atoms	17.2	36.9	23.1
Side chain atoms	19.9	39.5	26.5
Zn^{2+}	13.6(2)	24.9(2)	18.7(2)
Ca^{2+}	14.6(6)	41.4(6)	21.5(6)
Carbohydrate	54.2(139)	81.4(88)	37.4(226)
GM6001	16.2(56)	36.9(56)	0(-)
Water	26.5(668)	31.6(211)	22.2(151)
R.m.s deviations			
Bond lengths (Å)	0.0047	0.0065	0.0045
Bond angles (°)	1.20	1.44	1.14
Ramachandran plot			
Most favored	87.2%	84.3%	82.8%
Additional allowed	12.1%	15.0%	16.4%
Generously allowed	0.4%	0.6%	0.4%
Disallowed	0.1%(R297B)	0.1%(R297B)	0.3%(R297A/R297B)

[a]$R_{merge} = \Sigma_{hkl}\Sigma_i | I_i(hkl) - \langle I(hlk)\rangle | / \Sigma_{hkl}\Sigma_i I_i(hkl)$, where $I_i(hkl)$ is the *i*th intensity measurement of reflection *hkl* and $\langle I(hlk)\rangle$ is its average.
[b]$R_{work} = \Sigma | F_{obs} - F_{calc} | / \Sigma | F_{obs} |$.
[c]R_{free} = *R*-value for a randomly selected subset (5%) of the data that were not used for minimization of the crystallographic residual. A single crystal was used for measurement of each data set.

crystal contacts for the neighboring molecule, resulting in crystals that were distinct from the inhibitor-free form.

3.2. Overall structure

The overall structure of catrocollastatin/VAP2B is presented in Fig. 1. The structure of the M-domain was very similar to the corresponding structures in adamalysin II [15] and ADAM33 [17], with a flat elliptical shape and a core formed by a five-stranded β-sheet and four α-helices. A conserved methionine (Met357, Met-turn) was present downstream of the consensus HEXXHXXGXXHD sequence, which contains three histidines (His333, His337 and His343) that function as ligands of the catalytic zinc atom, and a glutamate residue (Glu334) that functions as the general base (Fig. 2). These structural features are typical of the metzincine family of metalloproteinases [30,31]. A bound calcium ion was identified opposite the active site cleft and close to the crossover point of the N- and C-terminal segments of the M-domain (Ca^{2+}-binding site I), as in the structures of adamalysin II [15] and ADAM33 [17]. The M-domain is followed by the D-domain, which can be sub-divided into "shoulder" (D_s) and "arm" (D_a) segments. D_s protrudes from the M-domain close to Ca^{2+}-binding site I, opposing the catalytic zinc atom. The C-domain is sub-divided into "wrist" (C_w) and "hand" (C_h) segments. Because of its curved structure, with the concave surface toward the M-domain, the distal portion of C_h comes close to and faces the catalytic site, thus the entire molecule adopts a C-shaped conformation. In the D_s and D_a segments, there are Ca^{2+} ions (sites II and III, respectively) that stabilize the structure. Details of the Ca^{2+}-coordinations are shown in Supplementary Fig. 2. The distal portion of the C-shape, spanning residues 561–582 of the C_h domain, is the region in which the amino acid sequence is most divergent and variable in length among ADAM/adamalysin/reprolysin family proteins (Fig. 2 and Supplementary Fig. 1). We designated this region as the hyper-variable-region (HVR), and have proposed that it represents a potential exosite for target recognition [19]. Aside from Cys377, whose side chain is embedded in the hydrophobic core, all 34 cysteinyl residues are involved in disulfide bonding. The number and spacing of cysteinyl residues, and the structures of the Ca^{2+}-binding sites are strictly conserved among ADAM/adamalysin/reprolysin family proteins (Fig. 2 and Supplementary Fig. 1). Fig. 2 shows the sequence alignment of a selected subset of ADAMs and SVMPs; alignment of the full sequences of catrocollastatin/VAP2B and 107 proteins of the ADAM/adamalysin/reprolysin family can be found in Supplementary Fig. 1.

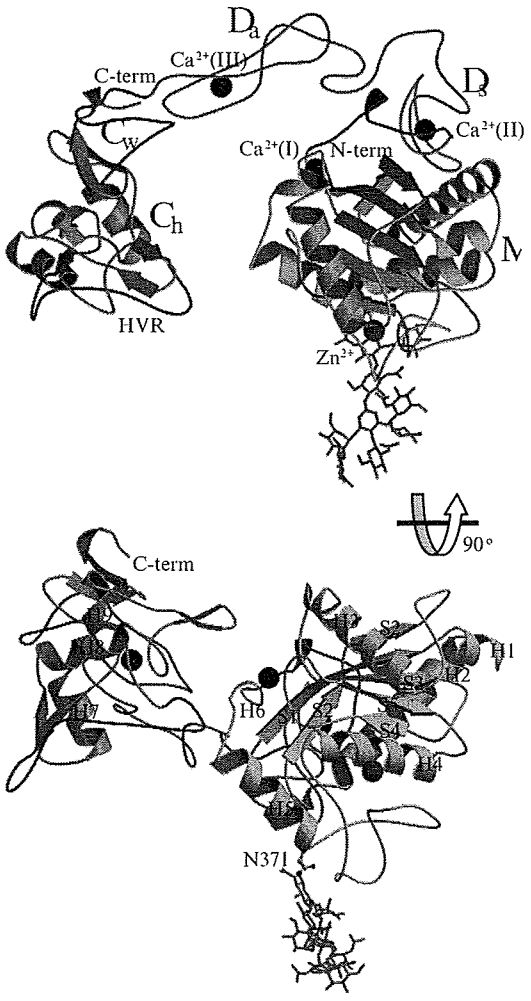

Fig. 1. Ribbon diagrams of catrocollastatin/VAP2B. The M-domain, linker, D_s, D_a, C_w, and C_h segments and the HVRs are shown in red, yellow, grey, cyan, pink, grey, green and blue, respectively. Zinc and calcium ions are represented as red and black spheres, respectively. The carbohydrate moiety linked to Asn371 is shown as a stick representation.

3.3. Flexible modular architecture

The structures of the M-domain (Fig. 3A), D_s (Fig. 3C), and C_w/C_h (Fig. 3B) of the six catrocollastatin/VAP2B molecules were nearly identical (r.m.s.d of 0.33, 0.45 and 0.59 Å, respectively). They were also essentially the same as the corresponding regions of VAP1 (r.m.s.d of 0.78, 0.63 and 1.1 Å, respectively (Fig. 3A–C)). However, the relative orientations of the sub-domains were quite variable. The largest difference was observed when the M domains of the six catrocollastatin/VAP2B molecules are superimposed. The $D_s/D_a/C_w/C_h$ portion should be rotated by approximately 13° relative to the M-domain, bringing about a 15-Å displacement at the distal end of C_h (Fig. 3A). A similar plot of the C_h segments superimposed shows less hinge bending, bringing approximately a 6-Å displacement at the distal portion of D_s (Fig. 3B). This conformed that the hinge motion occurs largely between the M domain and D_s. The bending of the main chain at two residues, Val403 and Gly438, is most prominent (Fig. 3C), however, the entire linker region (which is defined by the segment between two structural Ca^{2+}-binding sites, I and II) also moves in concert with the bending motion of Val403 (Fig. 3D). In this concerted movement of the linker, the side chain of Leu408 in D_s is positioned at a pivotal point (Fig. 3D and E). The main chain carbonyl oxygen atom of Leu408 coordinates the calcium ion at site II, whereas, the side-chain of Leu408 protrudes from D_s and interacts with a small hydrophobic cavity on the surface of the M domain (Fig. 3D). A balky hydrophobic residue (Leu or Phe or Tyr) at this position is highly conserved among ADAM/adamalysin/reprolysin family proteins (Supplementary Fig. 1), and its side chain probably functions as

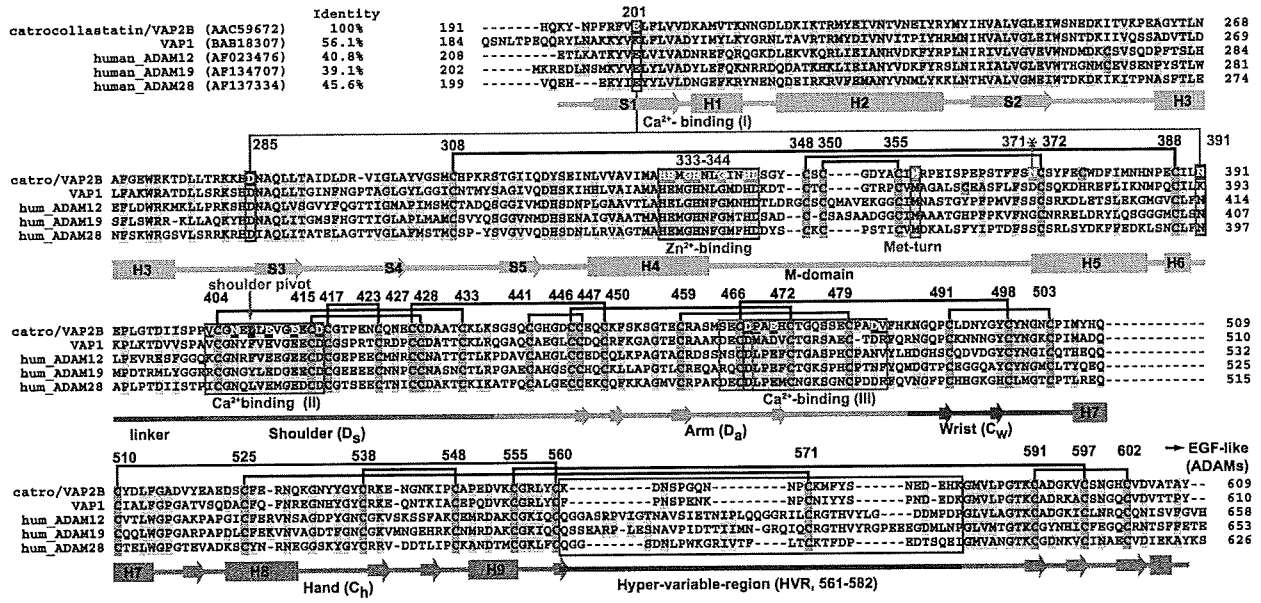

Fig. 2. Sequence alignment of catrocollastatin/VAP2B, VAP1 and human ADAMs. The cysteinyl residues and the conserved residues are shaded in pink and yellow, respectively. Disulfide bridges, secondary structures and domains are drawn schematically. The HVR, Ca^{2+}-binding sites, Zn^{2+}-binding site and disintegrin-loop are boxed in blue, red, green and cyan, respectively. The Ca^{2+}-coordinating residues are shaded in red.

a universal joint (shoulder joint) that allows D_s to adopt various orientations with respect to the M domain. The linker has fewer specific interactions with D_s and has a rather high B-factor (Supplementary Figs. 3 and 4). It is divergent and variable in length (7–12 aa), particularly in human ADAMs (Supplementary Fig. 1), thus may function primarily in connecting D_s to the M domain. The linker may also restrict the mobility of the shoulder joint, and thus determine the preferred orientation of the M domain of each ADAMs relative to the rest of the molecule for distinct targets. The residues forming the hydrophobic cavity with which Leu408 interacts are less conserved and also have relatively high B-factors (Supplementary Figs. 3 and 4). Thus they may also contribute to the flexibility of the shoulder joint.

Previously, we suggested a putative mechanism of HVR-mediated target recognition and catalysis by this family of proteins [19]. The present study allows us to incorporate into the previous model that intrinsic flexibility may be important for fine-tuning substrate recognition, by adjusting the spatial alignment of the catalytic and adhesion sites during the catalytic cycle (Fig. 3F). The structure of the lower half of the D_a segment in catrocollastatin/VAP2B was different from that of VAP1 (Fig. 3B and Supplementary Fig. 3C), most likely due to the substitution of Glu470 (in catrocollastain/VAP2B) with Asp471 (in VAP1), and the insertion of Pro480 (in catrocollastain/VAP2B). All the ADAMs, with the exception of ADAMs 10 and 17, which lack Ca^{2+}-binding site III, and the monomeric P-III and P-IV SVMPs contain Glu470 and Pro480 (see Supplementary Fig. 1). Thus, it is likely that they adopt a more catrocollastatin/VAP2B-like structure. As was observed in VAP1, the disintegrin-loop is packed by C_w, and forms a less flexible D_a/C_w junction, and therefore is unavailable for ligand binding. Differences in the orientation of D_a and C_w among these proteins may be important for proper spatial alignment of the catalytic and adhesion units and for substrate binding specificity. The angle between C_w and C_h in catrocollastatin/VAP2B was nearly invariant. It was essentially the same as that seen in VAP1 (Fig. 3B), but substantially different than that of ADAM10 [18,19]. Whether different ADAM/adamalysin/reprolysin family proteins have distinct C_w/C_h orientations remains to be established.

3.4. Modular architecture and post-translational processing

The disintegrins that are commonly found in Viperid venoms are typically generated by proteolytic processing of larger precursor molecules, the P-II class of SVMPs, which contain an M-domain plus a disintegrin portion [32,33]. The flexible modular structure described above points to a potential mechanism of selection of cleavage sites for this processing event. The cleavage sites of the medium-sized disintegrins (70 amino acids) are usually within Ca^{2+}-binding site II, whereas, those of the shorter ones (41–51 residues) are at the boundary between D_s and D_a. The longer disintegrins (84 residues) are processed within the linker between M and D_s (Fig. 4 and Supplementary Fig. 1). Most of the P-II SVMPs have fewer cysteine residues within their D_s segment (3 or 5 cysteine residues, see Supplementary Fig. 1) compared to P-III SVMPs, and thus have fewer disulfide bonds. Additionally, they contain substitutions of the calcium-binding residues at site II, indicating that they have a less stable D_s structure compared to P-III SVMPs. Long disintegrins have the same number of cysteine residues (7 cysteine residues) and Ca^{2+}-binding residues at site II as P-III SVMPs and ADAMs, and thus would be predicted to have a more stable D_s structure, which may account for their cleavage at the linker between M and D_s. A protective role for calcium against auto proteolysis in the linker region has been reported [34], and the linker region is usually removed from P-I SVMPs post-translationally [35]. Collectively, these observations suggest that differential susceptibility to proteolysis in the linker region and D_s, due to variability in the number of disulfide bonds and the presence or absence of bound calcium at site II, may underlie the

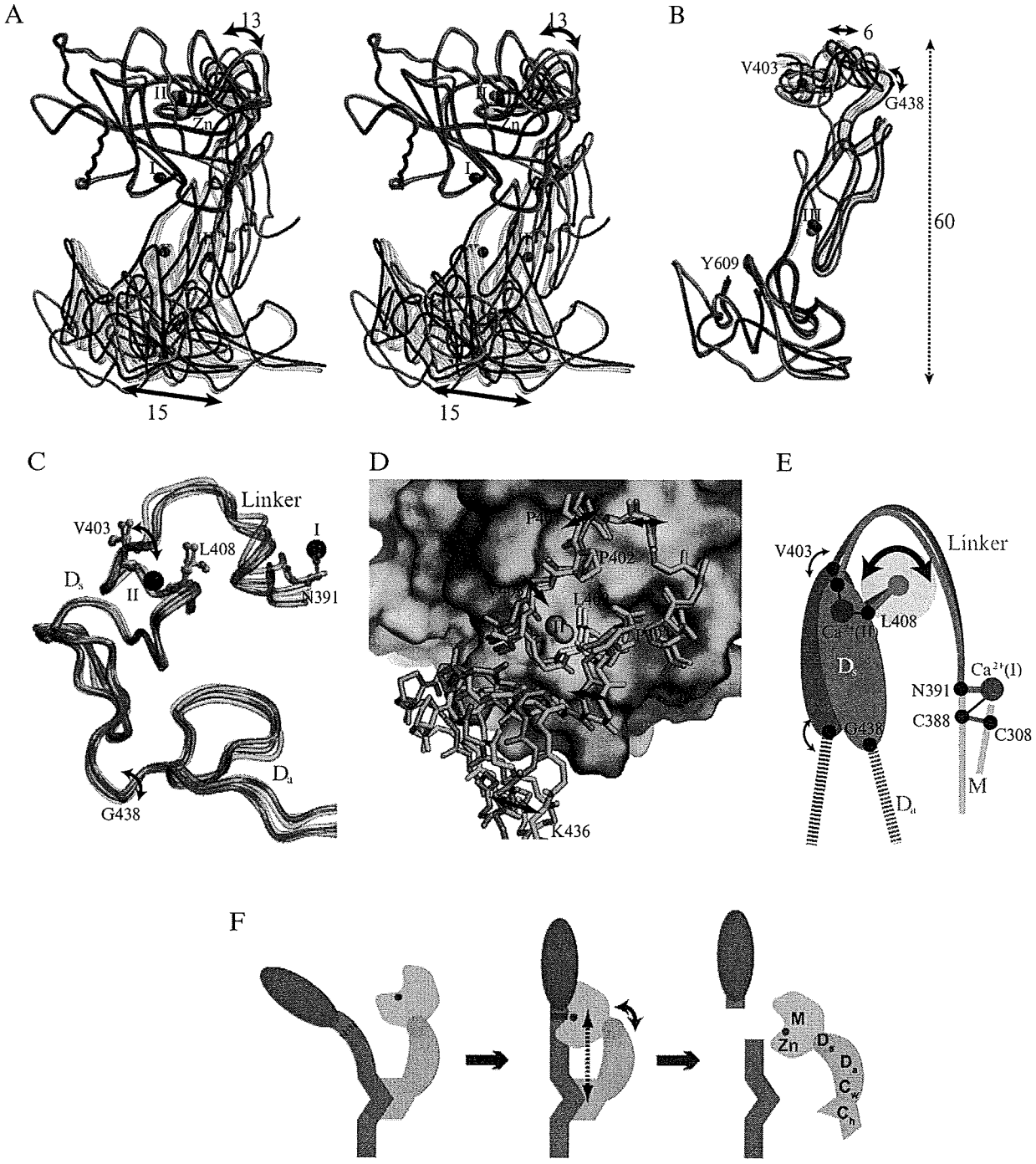

Fig. 3. Mobility of the sub-domains. (A) The M-domains of the six catrocollastatin/VAP2B molecules and the VAP1 monomer were superimposed and are shown in stereo. Two representative catrocollastatin/VAP2B molecules are shown in blue and red, the other four catrocollastatin/VAP2B molecules are in gray, and the VAP1 monomer is in green. The zinc ion is shown as a yellow sphere. The calcium atoms bound to the red and blue catrocollastatin/VAP2B molecule and VAP1 are shown as red, blue and green spheres, respectively. Superimposition of the D_h and C_s segments of the six catrocollastatin/VAP2B molecules and the VAP1 monomer are shown in B and C, respectively. (D) Close-up view of the shoulder joint. The molecular surface of the M-domain is colored according to the electrochemical surface potential (red to blue). The linker and part of the D_s segment of the two representative catrocollastatin/VAP2B molecules are shown as stick representations in pink and cyan, respectively. (E) Schematic diagram of the hinge motion at the shoulder joint. (F) Schematic model of substrate recognition and cleavage by a soluble ADAM/adamalysin/reprolysin protein.

generation of disintegrins with different lengths. Fertilin α (ADAM1) and β (ADAM2) undergo proteolytic processing within Ca^{2+}-binding site III and the linker region, respectively at different stages of sperm maturation (Fig. 4, Supplementary Fig. 1) [36,37]. The current structural data suggests that Ca^{2+}-binding, together with a flexible modular structure, may also

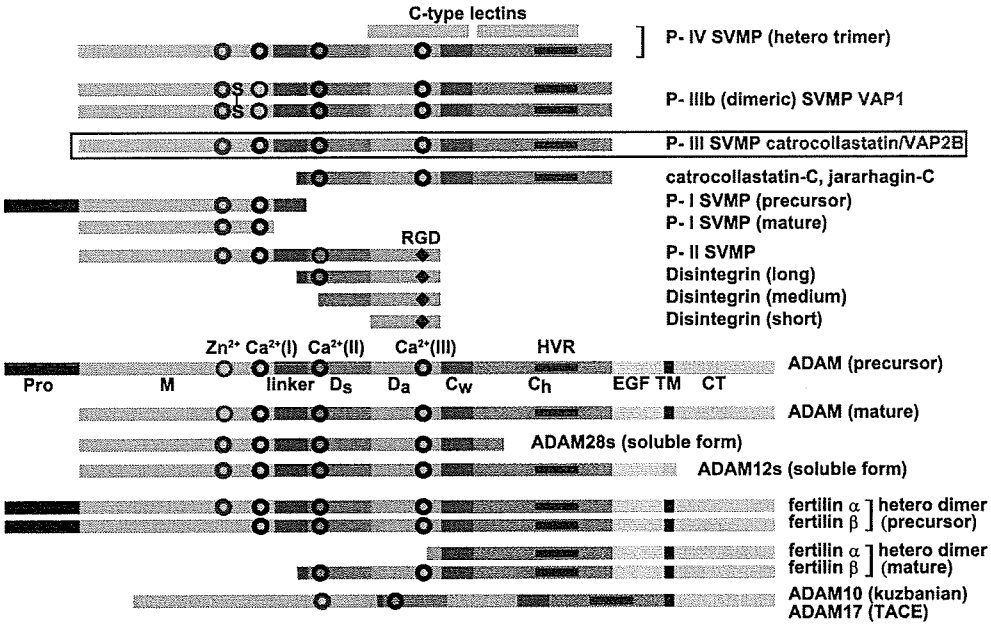

Fig. 4. Schematic representation of the modular architecture of ADAM/adamalysin/reprolysin family proteins. Each sub-domain is colored as for Fig. 1; the pro-domain (Pro), EGF-like domain (EGF), transmembrane region (TM) and cytoplasmic domain (CT) are in black, yellow, black and light salmon, respectively. The RGD sequences in disintegrins and an interchain disulfide bond in VAP1 are indicated. The Zn^{2+} and Ca^{2+} ions are shown as red and black circles, respectively; the closed circles indicate that all the members have a complete metal-binding sequence, whereas, open circles indicate that some members do not have it.

play a role in differential proteolytic processing of precursor proteins, giving rise to the biochemical and functional complexity of Crotalid and Viperid snake venoms, as well as post-translational regulation of ADAMs' functions.

4. Conclusion

ADAMs are widely distributed and constitute major membrane-bound sheddases that proteolytically process cell-surface-proteins for cell–cell communication. As such, they have emerged as potential therapeutic targets for a variety of diseases. SVMPs are key toxins involved in venom-induced pathogenesis, and thus are important targets for antivenom therapeutics. However, the physiological targets of ADAMs and SVMPs, and the molecular mechanism of target recognition are poorly understood. The structures presented here reveal a dynamic, modular architecture of the MDC domains of ADAM/adamalysin/reprolysin family proteins. Intrinsic flexibility may be important for fine-tuning substrate recognition, adjusting the spatial alignment of the catalytic and adhesion sites, and for post-translational regulation of this family of proteins.

Acknowledgement: We thank M. Tomisako for her help in crystallization experiments. This work was partly supported by Grant nano-001 for Research on Advanced Medical Technology from the Ministry of Health, Labor, and Welfare of Japan, and by grants from the Takeda Science Foundation, from the Kao Foundation for Arts and Science, from Mitsubishi Pharma Research Foundation and from Senri Life Science Foundation. T. I is supported by the grant from New Energy and Industrial Technology Development Organization (NEDO) of Japan.

Appendix A. Supplementary data

The atomic coordinates and structure factors have been deposited in the Protein Data Bank under accession codes 2DW0, 2DW1 and 2DW2 for the Form 2-1, Form 2-2 and Form 2-5 crystals, respectively. Supplementary data associated with this article can be found, in the online version, at doi:10.1016/j.febslet.2007.04.057.

References

[1] Gutierrez, J.M., Rucavado, A., Escalante, T. and Diaz, C. (2005) Hemorrhage induced by snake venom metalloproteinases: biochemical and biophysical mechanisms involved in microvessel damage. Toxicon 45, 997–1011.
[2] Araki, S., Ishida, T., Yamamoto, T., Kaji, K. and Hayashi, H. (1993) Induction of apoptosis by hemorrhagic snake venom in vascular endothelial cells. Biochem. Biophys. Res. Commun. 190, 148–153.
[3] Masuda, S., Araki, S., Yamamoto, T., Kaji, K. and Hayashi, H. (1997) Purification of a vascular apoptosis-inducing factor from hemorrhagic snake venom. Biochem. Biophys. Res. Commun. 235, 59–63.
[4] Masuda, S., Hayashi, H. and Araki, S. (1998) Two vascular apoptosis-inducing proteins from snake venom are members of the metalloprotease/disintegrin family. Eur. J. Biochem. 253, 36–41.
[5] Trummal, K. et al. (2005) A novel metalloprotease from Vipera lebetina venom induces human endothelial cell apoptosis. Toxicon 46, 46–61.
[6] Masuda, S., Hayashi, H., Atoda, H., Morita, T. and Araki, S. (2001) Purification, cDNA cloning and characterization of the vascular apoptosis-inducing protein, HV1, from Trimeresurus flavoviridis. Eur. J. Biochem. 268, 3339–3345.
[7] You, W.K., Seo, H.J., Chung, K.H. and Kim, D.S. (2003) A novel metalloprotease from Gloydius halys venom induces endothelial

cell apoptosis through its protease and disintegrin-like domains. J. Biochem. (Tokyo) 134, 739–749.
[8] Masuda, S., Ohta, T., Kaji, K., Fox, J.W., Hayashi, H. and Araki, S. (2000) cDNA cloning and characterization of vascular apoptosis-inducing protein 1. Biochem. Biophys. Res. Commun. 278, 197–204.
[9] Bjarnason, J.B. and Fox, J.W. (1995) Snake venom metalloendopeptidases: reprolysins. Meth. Enzymol. 248, 345–368.
[10] Fox, J.W. and Serrano, S.M. (2005) Structural considerations of the snake venom metalloproteinases, key members of the M12 reprolysin family of metalloproteinases. Toxicon 45, 969–985.
[11] Araki, S., Masuda, S., Maeda, H., Ying, M.J. and Hayashi, H. (2002) Involvement of specific integrins in apoptosis induced by vascular apoptosis-inducing protein 1. Toxicon 40, 535–542.
[12] Maruyama, J., Hayashi, H., Miao, J., Sawada, H. and Araki, S. (2005) Severe cell fragmentation in the endothelial cell apoptosis induced by snake apoptosis toxin VAP1 is an apoptotic characteristic controlled by caspases. Toxicon 46, 1–6.
[13] Seals, D.F. and Courtneidge, S.A. (2003) The ADAMs family of metalloproteases: multidomain proteins with multiple functions. Genes Dev. 17, 7–30.
[14] White, J.M. (2003) ADAMs: modulators of cell–cell and cell–matrix interactions. Curr. Opin. Cell. Biol. 15, 598–606.
[15] Gomis-Ruth, F.X., Kress, L.F. and Bode, W. (1993) First structure of a snake venom metalloproteinase: a prototype for matrix metalloproteinases/collagenases. EMBO J. 12, 4151–4157.
[16] Maskos, K. et al. (1998) Crystal structure of the catalytic domain of human tumor necrosis factor-alpha-converting enzyme. Proc. Natl. Acad. Sci. USA 95, 3408–3412.
[17] Orth, P. et al. (2004) Crystal structure of the catalytic domain of human ADAM33. J. Mol. Biol. 335, 129–137.
[18] Janes, P.W. et al. (2005) Adam meets Eph: an ADAM substrate recognition module acts as a molecular switch for ephrin cleavage in trans. Cell 123, 291–304.
[19] Takeda, S., Igarashi, T., Mori, H. and Araki, S. (2006) Crystal structures of VAP1 reveal ADAMs' MDC domain architecture and its unique C-shaped scaffold. EMBO J. 25, 2388–2396.
[20] Zhou, Q., Smith, J.B. and Grossman, M.H. (1995) Molecular cloning and expression of catrocollastatin, a snake-venom protein from *Crotalus atrox* (western diamondback rattlesnake) which inhibits platelet adhesion to collagen. Biochem. J. 307 (Pt 2), 411–417.
[21] Igarashi, T., Oishi, Y., Araki, S., Mori, H. and Takeda, S. (2006) Crystallization and preliminary X-ray crystallographic analysis of two vascular apoptosis-inducing proteins (VAPs) from *Crotalus atrox* venom. Acta Crystallogr. Sect. F Struct. Biol. Cryst. Commun. 62, 688–691.
[22] Otwinoski, Z. and Minor, W. (1997) in: Methods in Enzymology (Carter, C.W. and Sweet, R.M., Eds.), vol. 276, pp. 307-325.
[23] CCP4. (1994) The CCP4 suite: programs for protein crystallography. Acta Crystallogr. D Biol. Crystallogr. 50, 760–763.
[24] Roussel, A. and Cambillau, C. (1996) AFMB-CNRS, Marseille, France.
[25] Brunger, A.T. et al. (1998) Crystallography & NMR system: a new software suite for macromolecular structure determination. Acta Crystallogr. D Biol. Crystallogr. 54 (Pt 5), 905–921.
[26] Kraulis, P.J. (1991) MOLSCRIPT: a program to produce both detailed and schimatic plots of protein structure. Acta Crystallogr. D Biol. Crystallogr. 24, 946–950.
[27] Merritt, E.A.A.B. and David, J. (1997) in: Methods in Enzymology, vol. 277, pp. 505–524.
[28] DeLano, W.L. (2002) DeLano Scientific, San Carlos, CA, USA.
[29] Masuda, S., Maeda, H., Miao, J.Y., Hayashi, H. and Araki, S.-C. (2007) cDNA cloning and some additional peptide characterization of a single-chain vascular apoptosis-inducing protein, VAP2. Endothelium 14, 1–8.
[30] Bode, W., Gomis-Ruth, F.X. and Stockler, W. (1993) Astacins, serralysins, snake venom and matrix metalloproteinases exhibit identical zinc-binding environments (HEXXHXXGXXH and Met-turn) and topologies and should be grouped into a common family, the 'metzincins'. FEBS Lett. 331, 134–140.
[31] Gomis-Ruth, F.X. (2003) Structural aspects of the metzincin clan of metalloendopeptidases. Mol. Biotechnol. 24, 157–202.
[32] Kini, R.M. and Evans, H.J. (1992) Structural domains in venom proteins: evidence that metalloproteinases and non-enzymatic platelet aggregation inhibitors (disintegrins) from snake venoms are derived by proteolysis from a common precursor. Toxicon 30, 265–293.
[33] Calvete, J.J., Marcinkiewicz, C., Monleon, D., Esteve, V., Celda, B., Juarez, P. and Sanz, L. (2005) Snake venom disintegrins: evolution of structure and function. Toxicon 45, 1063–1074.
[34] Takeya, H., Nishida, S., Nishino, N., Makinose, Y., Omori-Satoh, T., Nikai, T., Sugihara, H. and Iwanaga, S. (1993) Primary structures of platelet aggregation inhibitors (disintegrins) autoproteolytically released from snake venom hemorrhagic metalloproteinases and new fluorogenic peptide substrates for these enzymes. J. Biochem. (Tokyo) 113, 473–483.
[35] Fox, J.W. and Bjarnason, J.B. (1995) Atrolysins: metalloproteinases from *Crotalus atrox* venom. Meth. Enzymol. 248, 368–387.
[36] Blobel, C.P., Myles, D.G., Primakoff, P. and White, J.M. (1990) Proteolytic processing of a protein involved in sperm-egg fusion correlates with acquisition of fertilization competence. J. Cell Biol. 111, 69–78.
[37] Blobel, C.P., Wolfsberg, T.G., Turck, C.W., Myles, D.G., Primakoff, P. and White, J.M. (1992) A potential fusion peptide and an integrin ligand domain in a protein active in sperm-egg fusion. Nature 356, 248–252.

J Appl Physiol 102: 622–627, 2007.
First published November 2, 2006; doi:10.1152/japplphysiol.00622.2006.

Hypothermia reduces ischemia- and stimulation-induced myocardial interstitial norepinephrine and acetylcholine releases

Toru Kawada,[1] Hirotoshi Kitagawa,[2] Toji Yamazaki,[2] Tsuyoshi Akiyama,[2] Atsunori Kamiya,[1] Kazunori Uemura,[1] Hidezo Mori,[2] and Masaru Sugimachi[1]

[1]*Department of Cardiovascular Dynamics, Advanced Medical Engineering Center, and*
[2]*Department of Cardiac Physiology, National Cardiovascular Center Research Institute, Osaka, Japan*

Submitted 4 June 2006; accepted in final form 1 November 2006

Kawada T, Kitagawa H, Yamazaki T, Akiyama T, Kamiya A, Uemura K, Mori H, Sugimachi M. Hypothermia reduces ischemia- and stimulation-induced myocardial interstitial norepinephrine and acetylcholine releases. *J Appl Physiol* 102: 622–627, 2007. First published November 2, 2006; doi:10.1152/japplphysiol.00622.2006.—Although hypothermia is one of the most powerful modulators that can reduce ischemic injury, the effects of hypothermia on the function of the cardiac autonomic nerves in vivo are not well understood. We examined the effects of hypothermia on the myocardial interstitial norepinephrine (NE) and ACh releases in response to acute myocardial ischemia and to efferent sympathetic or vagal nerve stimulation in anesthetized cats. We induced acute myocardial ischemia by coronary artery occlusion. Compared with normothermia ($n = 8$), hypothermia at 33°C ($n = 6$) suppressed the ischemia-induced NE release [63 nM (SD 39) vs. 18 nM (SD 25), $P < 0.01$] and ACh release [11.6 nM (SD 7.6) vs. 2.4 nM (SD 1.3), $P < 0.01$] in the ischemic region. Under hypothermia, the coronary occlusion increased the ACh level from 0.67 nM (SD 0.44) to 6.0 nM (SD 6.0) ($P < 0.05$) and decreased the NE level from 0.63 nM (SD 0.19) to 0.40 nM (SD 0.25) ($P < 0.05$) in the nonischemic region. Hypothermia attenuated the nerve stimulation-induced NE release from 1.05 nM (SD 0.85) to 0.73 nM (SD 0.73) ($P < 0.05$, $n = 6$) and ACh release from 10.2 nM (SD 5.1) to 7.1 nM (SD 3.4) ($P < 0.05$, $n = 5$). In conclusion, hypothermia attenuated the ischemia-induced NE and ACh releases in the ischemic region. Moreover, hypothermia also attenuated the nerve stimulation-induced NE and ACh releases. The Bezold-Jarisch reflex evoked by the left anterior descending coronary artery occlusion, however, did not appear to be affected under hypothermia.

vagal nerve; sympathetic nerve; cardiac microdialysis; cats

HYPOTHERMIA IS ONE OF THE most powerful modulators that can reduce ischemic injury in the central nervous system, heart, and other organs. The general consensus is that hypothermia induces a hypometabolic state in tissues and balances energy supply and demand (25). With respect to the myocardial ischemia, the size of a myocardial infarction correlates with temperature (6), and mild hypothermia can protect the myocardium against acute ischemic injury (9). The effects of hypothermia on the function of the cardiac autonomic nerves in terms of neurotransmitter releases, however, are not fully understood. Because autonomic neurotransmitters such as norepinephrine (NE) and ACh directly impinge on the myocardium, they would be implicated in the cardioprotection by hypothermia.

In previous studies from our laboratory, Kitagawa et al. (16) demonstrated that hypothermia attenuated the nonexocytotic NE release induced pharmacologically by ouabain, tyramine, or cyanide. Kitagawa et al. (15) also demonstrated that hypothermia attenuated the exocytotic NE release in response to vena cava occlusion or to local administration of high K^+. The effects of hypothermia on the ischemia-induced myocardial interstitial NE release, however, were not examined in those studies. In addition, the effects of hypothermia on the ischemia-induced myocardial interstitial ACh release have never been examined. Because both sympathetic and parasympathetic nerves control the heart, simultaneous monitoring of the myocardial interstitial releases of NE and ACh (14, 31) would help integrative understanding of the autonomic nerve terminal function under hypothermia in conjunction with acute myocardial ischemia.

In the present study, the effects of hypothermia on the ischemia-induced and nerve stimulation-induced myocardial interstitial neurotransmitter releases were examined. We implanted a dialysis probe into the left ventricular free wall of anesthetized cats and measured dialysate NE and ACh levels as indexes of neurotransmitter outputs from the cardiac sympathetic and vagal nerve terminals, respectively. Based on our laboratory's previous results (15, 16), we hypothesized that hypothermia would attenuate the neurotransmitter releases in response to acute myocardial ischemia and to electrical nerve stimulation.

MATERIALS AND METHODS

Surgical Preparation and Protocols

Animals were cared for in accordance with the *Guiding Principles for the Care and Use of Animals in the Field of Physiological Sciences*, approved by the Physiological Society of Japan. All protocols were reviewed and approved by the Animal Subjects Committee of National Cardiovascular Center. Adult cats were anesthetized via an intraperitoneal injection of pentobarbital sodium (30–35 mg/kg) and ventilated mechanically through an endotracheal tube with oxygen-enriched room air. The level of anesthesia was maintained with a continuous intravenous infusion of pentobarbital sodium (1–2 $mg \cdot kg^{-1} \cdot h^{-1}$) through a catheter inserted from the right femoral vein. Mean arterial pressure (MAP) was measured using a pressure transducer connected to a catheter inserted from the right femoral artery. Heart rate (HR) was determined from an electrocardiogram.

Protocol 1: acute myocardial ischemia. We examined the effects of hypothermia on the ischemia-induced myocardial interstitial releases of NE and ACh. The heart was exposed by partially removing the left fifth and/or sixth rib. A dialysis probe was implanted transversely into

Address for reprint requests and other correspondence: T. Kawada, Dept. of Cardiovascular Dynamics, Advanced Medical Engineering Center, National Cardiovascular Center Research Institute, 5-7-1 Fujishirodai, Suita, Osaka 565-8565, Japan (e-mail: torukawa@res.ncvc.go.jp).

The costs of publication of this article were defrayed in part by the payment of page charges. The article must therefore be hereby marked "*advertisement*" in accordance with 18 U.S.C. Section 1734 solely to indicate this fact.

the anterolateral free wall of the left ventricle perfused by the left anterior descending coronary artery (LAD) to monitor myocardial interstitial NE and ACh levels in the ischemic region during occlusion of the LAD (13). Another dialysis probe was implanted transversely into the posterior free wall of the left ventricle perfused by the left circumflex coronary artery to monitor myocardial interstitial NE and ACh levels in a nonischemic region. Heparin sodium (100 U/kg) was administered intravenously to prevent blood coagulation. Animals were divided into a normothermic group (n = 8) and a hypothermic group (n = 6). In the hypothermic group, surface cooling with ice bags was performed until the esophageal temperature decreased to 33°C (15, 16). A stable hypothermic condition was obtained within ~2 h. In each group, we occluded the LAD for 60 min and examined changes in the myocardial interstitial NE and ACh levels in the ischemic region (i.e., the LAD region) and nonischemic region (i.e., the left circumflex coronary artery region). Fifteen-minute dialysate samples were obtained during the preocclusion baseline condition and during the periods of 0–15, 15–30, 30–45, and 45–60 min of the LAD occlusion.

Protocol 2: sympathetic stimulation. We examined the effects of hypothermia on the sympathetic nerve stimulation-induced myocardial interstitial NE release (n = 6). A dialysis probe was implanted transversely into the anterolateral free wall of the left ventricle. The bilateral cardiac sympathetic nerves originating from the stellate ganglia were exposed through a second intercostal space and sectioned. The cardiac end of each sectioned nerve was placed on a bipolar platinum electrode for sympathetic stimulation (5 Hz, 10 V, 1-ms pulse duration). The electrodes and nerves were covered with mineral oil to provide insulation and prevent desiccation. A 4-min dialysate sample was obtained during the sympathetic stimulation under the normothermic condition. Thereafter, hypothermia was introduced using the same cooling procedure as in *protocol 1*, and a second 4-min dialysate sample was obtained during the sympathetic stimulation.

Protocol 3: vagal stimulation. We examined the effects of hypothermia on the vagal nerve stimulation-induced ACh release (n = 5). A dialysis probe was implanted transversely into the anterolateral free wall of the left ventricle. The bilateral vagi were exposed through a midline cervical incision and sectioned at the neck. The cardiac end of each sectioned nerve was placed on a bipolar platinum electrode for vagal stimulation (20 Hz, 10 V, 1-ms pulse duration). To prevent severe bradycardia and cardiac arrest, which can be induced by the vagal stimulation, the heart was paced at 200 beats/min using pacing wires attached to the apex of the heart during the stimulation period. A 4-min dialysate sample was obtained during the vagal stimulation under the normothermic condition. Thereafter, hypothermia was introduced using the same cooling procedure as in *protocol 1*, and a second 4-min dialysate sample was obtained during the vagal stimulation.

Because of the relatively intense stimulation of the sympathetic or vagal nerve, the stimulation period in *protocols 2* and *3* was limited to 4 min to minimize gradual waning of the stimulation effects. At the end of the experiment, the animals were killed by increasing the depth of anesthesia with an overdose of pentobarbital sodium. We then confirmed that the dialysis probes had been threaded in the middle layer of the left ventricular myocardium.

Dialysis Technique

The dialysate NE and ACh concentrations were measured as indexes of myocardial interstitial NE and ACh levels, respectively. The materials and properties of the dialysis probe have been described previously (2, 3). Briefly, we designed a transverse dialysis probe. A dialysis fiber (13-mm length, 310-μm outer diameter, 200-μm inner diameter; PAN-1200, 50,000 molecular weight cutoff; Asahi Chemical) was connected at both ends to polyethylene tubes (25-cm length, 500-μm outer diameter, 200-μm inner diameter). The dialysis probe was perfused with Ringer solution containing a cholinesterase inhibitor eserine (10^{-4} M) at a rate of 2 μl/min. We started dialysate sampling from 2 h after the implantation of the dialysis probe(s), when the dialysate NE and ACh concentrations had reached steady states. The actual dialysate sampling was delayed by 5 min from the collection period to account for the dead space volume between the semipermeable membrane and the sample tube. Each sample was collected in a microtube containing 3 μl of HCl to prevent amine oxidation. The dialysate ACh concentration was measured directly by HPLC with electrochemical detection (Eicom). The in vitro recovery rate of ACh was ~70%. With the use of a criterion of signal-to-noise ratio of higher than three, the detection limit for ACh was 3 pg per injection. The dialysate NE concentration was measured by another HPLC-electrochemical detection system after the removal of interfering compounds by an alumina procedure. The in vitro recovery rate of NE was ~55%. With the use of a criterion of signal-to-noise ratio of higher than three, the detection limit for NE was 200 fg per injection.

Statistical Analysis

All data are presented as means and SD values. For *protocol 1*, we performed two-way repeated-measures ANOVA using hypothermia as one factor and the dialysate sampling periods (the effects of ischemia) as the other factor. For *protocols 2* and *3*, we compared stimulation-induced releases of NE and ACh before and during hypothermia using a paired t-test. For all of the statistics, the difference was considered significant when $P < 0.05$.

RESULTS

Figure 1*A* illustrates changes in myocardial interstitial NE levels in the ischemic region during LAD occlusion obtained from *protocol 1*. The *inset* shows the magnified ordinate for the

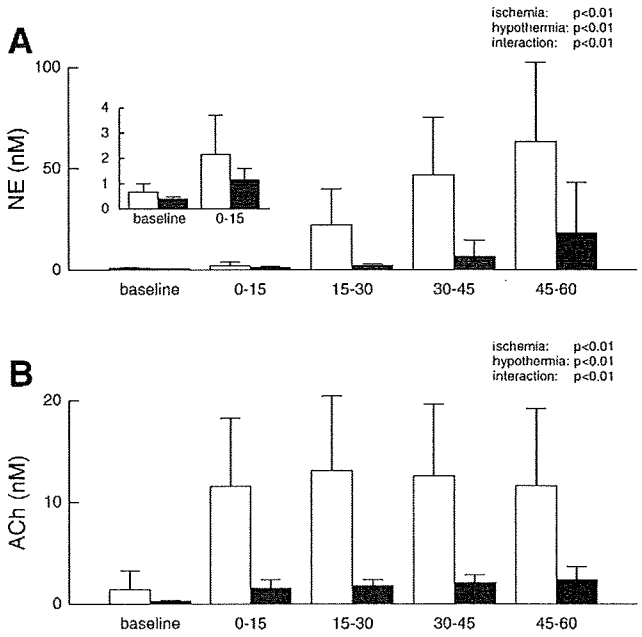

Fig. 1. *A*: ischemia-induced myocardial interstitial norepinephrine (NE) release in the ischemic region. Acute myocardial ischemia caused a progressive increase in the level of myocardial interstitial NE. Hypothermia attenuated the ischemia-induced NE release. *Inset*: magnified ordinate for the baseline and the 0- to 15-min period of ischemia. *B*: ischemia-induced myocardial interstitial ACh release in the ischemic region. Acute myocardial ischemia increased the myocardial interstitial ACh levels. Hypothermia attenuated the ischemia-induced ACh release. Open bars: normothermia; solid bars: hypothermia.

baseline and the 0- to 15-min period of ischemia. In the normothermic group (open bars), the LAD occlusion caused an ~94-fold increase in the NE level during the 45- to 60-min interval. In the hypothermic group (solid bars), the LAD occlusion caused an ~45-fold increase in the NE level during the 45- to 60-min interval. Compared with normothermia, hypothermia suppressed the baseline NE level to ~59% and the NE level during the 45- to 60-min period to ~29%. Statistical analysis indicated that the effects of both hypothermia and ischemia on the NE release were significant, and the interaction between hypothermia and ischemia was also significant.

Figure 1*B* illustrates changes in myocardial interstitial ACh levels in the ischemic region during the LAD occlusion. In both the normothermic (open bars) and hypothermic (solid bars) groups, the LAD occlusion caused an approximately eightfold increase in the ACh level during the 45- to 60-min interval. Compared with normothermia, however, hypothermia suppressed both the baseline ACh level and the ACh level during the 45- to 60-min period of ischemia to ~20%. Statistical analysis indicated that the effects of both hypothermia and ischemia on the ACh release were significant, and the interaction between hypothermia and ischemia was also significant.

Figure 2*A* illustrates changes in myocardial interstitial NE levels in the nonischemic region during the LAD occlusion. Note that scale of the ordinate is only one-hundredth of that in Fig. 1*A*. The LAD occlusion decreased the NE level in the normothermic group (open bars); the NE level during the 45- to 60-min interval was ~59% of the baseline level. The LAD occlusion also decreased the NE level in the hypothermic group (solid bars); the NE level during the 45- to 60-min interval was ~64% of the baseline level. Although the LAD occlusion resulted in a decrease in the NE level under both conditions, the NE level under hypothermia was nearly twice that measured under normothermia. The statistical analysis indicated that the effects of both hypothermia and ischemia on the NE release were significant, whereas the interaction between hypothermia and ischemia was not significant.

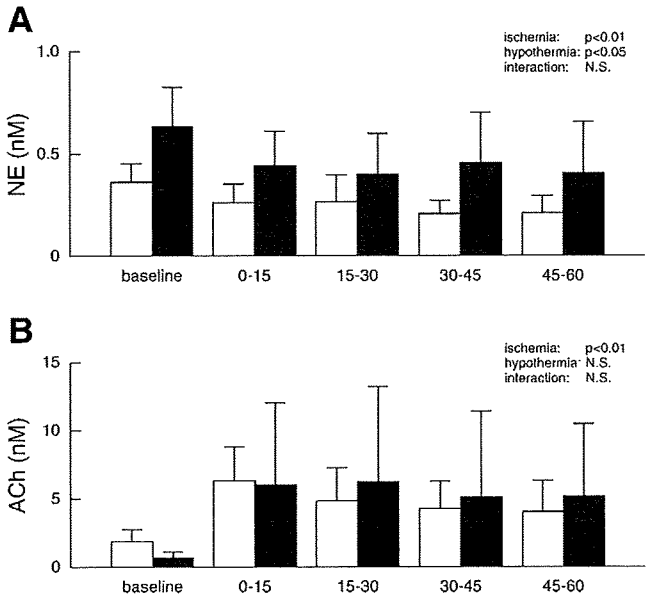

Fig. 2. *A*: changes in the myocardial interstitial NE levels in the nonischemic region. Acute myocardial ischemia decreased the level of myocardial interstitial NE from the baseline level. Hypothermia increased the myocardial interstitial NE levels in the nonischemic region. *B*: changes in the myocardial interstitial ACh levels in the nonischemic region. Acute myocardial ischemia increased the myocardial interstitial ACh level. Hypothermia did not attenuate the increasing response of ACh to the left anterior descending coronary artery occlusion. Open bars: normothermia; solid bars: hypothermia. NS, not significant.

Table 1. *Mean arterial pressure during acute myocardial ischemia obtained in protocol 1*

	Baseline	5 min	15 min	30 min	45 min	60 min
Normothermia	108 (23)	102 (28)	101 (24)	101 (20)	102 (21)	102 (21)
Hypothermia	108 (11)	80 (17)	87 (10)	85 (10)	86 (10)	91 (11)

Values are means (SD) (in mmHg) obtained during preocclusion baseline period and 5-, 15-, 30-, 45-, and 60-min periods of coronary artery occlusion. Ischemia: $P < 0.01$; hypothermia: not significant; interaction: $P < 0.01$.

Figure 2*B* illustrates changes in myocardial interstitial ACh levels in the nonischemic region during the LAD occlusion. The LAD occlusion caused an ~3.4-fold increase in the ACh level during the 0- to 15-min interval in the normothermic group (open bars). The LAD occlusion caused an approximately ninefold increase in the ACh level during the 0- to 15-min interval in the hypothermic group (solid bars). These effects of ischemia on the ACh release were statistically significant. Although hypothermia seemed to attenuate the baseline ACh level, the overall effects of hypothermia on the ACh level were insignificant.

Tables 1 and 2 summarize the MAP and HR data, respectively, obtained in *protocol 1*. Acute myocardial ischemia significantly reduced MAP ($P < 0.01$) and HR ($P < 0.01$). Hypothermia did not affect MAP but did decrease HR ($P < 0.01$). The interaction between ischemia and hypothermia was significant for MAP but not for HR by the two-way repeated-measures ANOVA.

For *protocol 2*, hypothermia significantly attenuated the sympathetic stimulation-induced NE release to ~70% of the level observed during normothermia (Fig. 3*A*). Under normothermia, the sympathetic stimulation increased MAP from 114 mmHg (SD 27) to 134 mmHg (SD 33) ($P < 0.01$) and HR from 147 beats/min (SD 9) to 207 beats/min (SD 5) ($P < 0.01$). Under hypothermia, the sympathetic stimulation increased MAP from 117 mmHg (SD 11) to 136 mmHg (SD 22) ($P < 0.05$) and HR from 125 beats/min (SD 16) to 164 beats/min (SD 10) ($P < 0.01$).

For *protocol 3*, hypothermia significantly attenuated the vagal stimulation-induced ACh release to ~70% of the level observed during normothermia (Fig. 3*B*). Hypothermia did not change MAP [117 mmHg (SD 18) vs. 118 mmHg (SD 27)] but

Table 2. *Heart rate during acute myocardial ischemia obtained in protocol 1*

	Baseline	5 min	15 min	30 min	45 min	60 min
Normothermia	183 (26)	160 (18)	163 (16)	163 (18)	166 (20)	165 (21)
Hypothermia	146 (25)	116 (19)	113 (19)	126 (39)	112 (20)	97 (31)

Values are means (SD) (in beats/min) obtained during preocclusion baseline period and 5-, 15-, 30-, 45-, and 60-min periods of coronary artery occlusion. Ischemia: $P < 0.01$; hypothermia: $P < 0.01$; interaction: not significant.